

# Gravity Effect of Alpine Slab Segments Based on Geophysical and Petrological Modelling

Maximilian Lowe<sup>1,2,3</sup>, Jörg Ebbing<sup>1</sup>, Amr El-Sharkawy<sup>1,4</sup>, Thomas Meier<sup>1</sup>

<sup>1</sup> Institute for Geosciences, Kiel University, Germany

<sup>2</sup> NERC British Antarctic Survey, Cambridge, United Kingdom

<sup>3</sup> School of geosciences, University of Edinburgh, United Kingdom

<sup>4</sup> National Research Institute of Astronomy and Geophysics (NRIAG), 11421, Helwan, Cairo, Egypt

Correspondence to Maximilian Lowe: maxwe32@bas.ac.uk

## Abstract

In this study, we present an estimate of the gravity signal of the slabs beneath the Alpine mountain belt. Estimates of the gravity effect of the subducting slabs are often omitted or simplified in crustal scale models. The related signal is here calculated for alternative slab configurations at near surface height and on a satellite altitude of 225 km.

We apply three different modelling approaches in order to estimate the gravity signal from the subducting slab segments, by: i) Direct conversion of upper mantle seismic velocities to density distribution, which are then forward calculated to obtain the gravity signal. ii) Definition of slab geometries based on seismic crustal thickness and high-resolution upper mantle tomography for two competing slab configurations. The geometries are then forward calculated by assigning a constant density contrast and slab thickness. iii) Accounting for compositional and thermal variations with depth within the predefined slab geometry.

Forward calculations predict a gravity signal of up to 40 mGal for the Alpine slab configuration. Significant differences in the gravity anomaly patterns are visible for different slab geometries in the near surface gravity field. However, different contributing slab segments are not easily separated, especially at satellite altitude. Our results demonstrate that future studies addressing the lithospheric structure of the Alps should have to account for the subducting slabs in order to provide a meaningful representation of the geodynamic complex Alpine area.

Keywords:

Satellite gravity gradient, Alpine subduction, lithospheric and sub lithospheric structure, mantle composition, seismic tomography

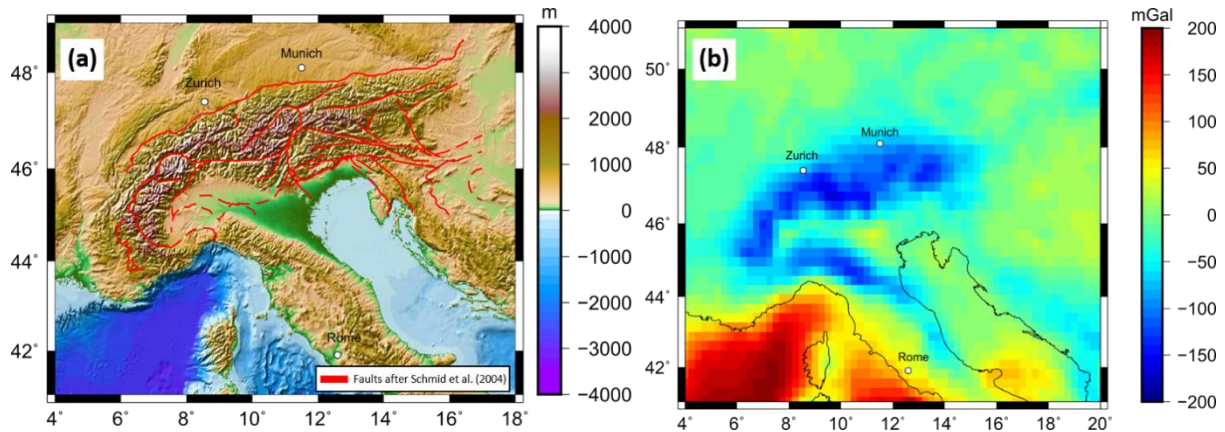
## 1. Introduction

Interpretation of gravity anomalies can reveal information on the architecture and tectonic setting of the lithosphere (e.g. Zeyen, & Fernández, 1994; McKenzie & Fairhead, 1997; Holzrichter & Ebbing, 2006; Braitenberg, 2015; Spooner et al. 2019). For subduction zones, like the Andes, several studies have shown that the gravity effect of the subducting plates is significant and has to be considered in order to study the feedback between the subducting lithosphere and the overriding plate (Götze et al. 1994; Götze & Krause 2002; Tašárová 2007 Gutknecht et al. 2014; Götze & Pail 2018; Mahatsente 2019). For lithosphere to subduct, a higher density than the surrounding mantle material at the same depth interval is required,

43 causing a negative buoyancy for the slab and therefore the slab is subducted into earth's interior  
44 (e.g. Kincaid & Olson 1987; Ganguly et al. 2009). However, the gravitational contribution of  
45 subducting material in the upper mantle to the gravity field has so far not been systematically  
46 addressed for the Alpine system. In order to provide an assessment, the magnitude of the gravity  
47 signal of such sub-crustal long wavelength features has to be estimated.

48 The Alpine mountain belt (Fig. 1a) is chosen for this sensitivity study because firstly a large  
49 range of recent seismic tomography studies imaged subducting slab segments in the Alpine  
50 region (e.g. Babuska et al., 1990; Lippitsch et al., 2003; Spakman & Wortel, 2004; Mitterbauer  
51 et al. 2011; Karousová et al., 2013; Zhao et al., 2016; Kästle et al., 2018; El-Sharkawy et al.,  
52 2020). Those different studies suggest different configurations of slab segments (see section  
53 1.1), allowing us to test how sensitive the gravity field is to varying geometries of subducting  
54 slab segments. Secondly, previous Alpine models addressing the Alpine gravity field have  
55 considered the subcrustal mantle inhomogeneities in form of lithosphere thickness (e.g. Ebbing  
56 et al., 2006; Spooner et al., 2019) or in form of mantle density variations (Tadiello and  
57 Braitenberg 2021), but without identifying the isolated effect of subducting slabs segments in  
58 the velocity or density variations. If the contribution of the mantle density variations is not  
59 considered, a significant part of the gravity field might be attributed to crustal thickness  
60 variations or intra-crustal sources.

61 In addition, the Bouguer Anomaly of the Alps (Fig. 1b) shows no direct sign of subducting slabs  
62 (in contrast to the Andes subduct zone) as the field is dominated by crustal thickness variations  
63 (Ebbing et al., 2001, 2006). Therefore, forward modeling of the proposed slab geometries, as  
64 imaged by high-resolution tomographic studies, is **necessary** to separate the gravity signal  
65 caused by the subducting slabs from the gravity **anomaly** field.



66

67 *Figure 1 (a) Topography from ETOPO1 from Amante and Eakins (2009). Faults in red after Schmid et al. (2004). (b) Bouguer*  
 68 *Anomaly based on XGM 2019 (Zingerle et al., 2020) with a maximum spherical harmonics degree of 719 at a station height of*  
 69 *6040m above the ellipsoid, just above the surface of the Alps. Correction density for rock: 2670 kg/m<sup>3</sup> and for water: 1030*  
 70 *kg/m<sup>3</sup>*

71 We present three different approaches to model the gravity effect of the slab segments and  
 72 discuss the strengths and limitations of the applied methods. In the first approach, the alpine  
 73 sup-crustal density distribution is derived by converting seismic velocities to density. This  
 74 model is then forward calculated to estimate the gravity response. In the second approach, 3D  
 75 slab geometries are derived by evaluating seismic crustal thickness estimations and high-  
 76 resolution upper mantle tomographic models. Here, two competing slab configurations are  
 77 chosen. The predefined slab geometries are then forward calculated by assigning different  
 78 density contrasts and slab thicknesses. The third approach uses similar predefined slab  
 79 configurations as in the second approach, however, here we consider petrology, temperature,  
 80 and density variation. The gravity response is calculated for all three approaches at a near  
 81 surface height for the gravity disturbance and the gravity gradients at satellite altitude of 225  
 82 km.

### 83 1.1 Alpine setting

84 The formation and present geodynamics of the Alps are linked to long lasting tectonic  
 85 processes, including Adria-Europe continent-continent collision, subduction of oceanic and  
 86 continental lithosphere, the formation of crustal nappes as well as **extensional and**  
 87 **compressional** processes (Frisch, 1979; Stampfli & Borel, 2002; Handy, et al., 2010, 2015).

88 The Adriatic microplate is a major driver of the present geodynamics in the Alpine region,

89 which is trapped between the converging major plates of Europe and Africa. Adria is moving  
90 counterclockwise with respect to Europe, as seen by GPS observations (e.g. Nocquet and Calais,  
91 2004; Vrabec and Fodor, 2006; Serpelloni et al., 2016) and is subducted beneath the Apennines  
92 to the west as well as to the east beneath the Dinarides, while colliding with Eurasia in the Alps  
93 to the north (e.g. Channel & Horvath, 1976; Dewey et al., 1989; Stampfli & Borel, 2002; Handy  
94 et al., 2010; Le Breton et al., 2017). Subducting slab segments have been imaged by different  
95 seismological body wave travel time tomographic studies as well as surface wave tomographic  
96 studies within the Alpine upper mantle (e.g. Babuska et al., 1990; Lippitsch et al., 2003;  
97 Spakman & Wortel, 2004; Mitterbauer et al. 2011; Karousová et al., 2013; Zhao et al., 2016;  
98 Kästle et al., 2018; El-Sharkawy et al., 2020). However, the configuration of subducting slab  
99 segments remains controversial. In the Western Alps, Lippitsch et al. (2003) propose a slab  
100 break-off at about 100 km depth, which is in line with the findings of Beller et al. (2018), Kästle  
101 et al. (2018) and El-Sharkawy et al. (2020). In contrast, a continuous subducting slab segment  
102 in the Western Alps, down to at least 250 km depth, is imaged by a number of other tomographic  
103 models (e.g. Koulakov et al., 2009; Zhao et al., 2016; Hua et al., 2017; Lyu et al., 2017).

104 A continuous subduction of Eurasia beneath the Central Alps down to at least 200 km depth is  
105 imaged by different tomographic models (e.g. Lippitsch et al., 2003; Piromallo and Morelli,  
106 2003; Koulakov et al., 2009; Mitterbauer et al., 2011; Hua et al., 2017; Fichtner et al., 2018; El-  
107 Sharkawy et al., 2020). A potential slab gap with an approximate size of 2° is separating the  
108 subducting slab segments in the Central Alps to the Eastern Alps as imaged by e.g. Lippitsch  
109 et al. (2003). The slab configuration and subduction direction in the Eastern Alps remains  
110 unclear. According to the classical view, Eurasia is subducting beneath Adria in a southward  
111 subduction (Hawkesworth et al., 1975; Lüschen et al., 2004; 2006). This idea was challenged  
112 by Lippitsch et al. (2003), Schmid et al. (2004), Kissling et al. (2006), Handy et al. (2015), and  
113 Hetenyi et al. (2018). Instead, slab break-off in the eastern Alps and a northward-dipping  
114 Adriatic slab in the easternmost Alps is suggested, leading to a switch of the slab polarity, as

115 Adria is subducting beneath the European plate (Handy et al., 2015). The view that Adriatic and  
116 not Eurasian lithosphere is subducting northwards in the Eastern Alps has been opposed by  
117 Mitterbauer et al. (2011), as their model shows a northward dipping slab in the eastern most  
118 Alps connected to the European plate. In an early tomographic study, Babuska et al. (1990)  
119 proposed that both Eurasian and Adriatic lithosphere is subducting in the eastern Alps. In  
120 subsequent studies and interpretations this model was mentioned but northward subduction of  
121 Adria seems to be favoured (e.g. Karousová et al., 2013; Hetenyi et al., 2018). Recently,  
122 subduction of both Eurasian and Adriatic lithosphere in the eastern Alps down to about 150 km  
123 has been suggested by Kästle et al. (2020) and El-Sharkawy et al. (2020) based on surface wave  
124 studies. For a more in-depth comparison and discussion of tomographic Alpine models the  
125 reader is referred to e.g. Kästle et al. (2020).

## 126 **2. Data**

127 The Bouguer Anomaly (Fig. 1b) is based on the global model *XGM 2019* (Zingerle et al., 2020)  
128 developed for spherical harmonics up to degree 719, with a resolution of  $\sim 25$  km (half  
129 wavelength). The *XGM 2019* model is a global integrated gravity model, which includes  
130 satellite and terrestrial measurements. The Bouguer Anomaly is calculated from the Free-Air  
131 gravity disturbance with a correction density of  $2670 \text{ kg/m}^3$  for topography, and a correction  
132 density for water of  $1030 \text{ kg/m}^3$  for the offshore areas using Tesseroids (Uieda et al., 2016). For  
133 the tesseroids, we use the topography and bathymetry from ETOPO (Amante & Eakins, 2009),  
134 which was regridded at a regular grid with a grid space of 25 km to match the resolution of the  
135 *XGM 2019* model for a maximum degree of 719. The gravity field is defined at a constant  
136 station height of 6040 m above the ellipsoid, just above the surface of the Alps. The resulting  
137 Bouguer Anomaly shows a gravity low in the order of  $-200 \text{ mGal}$  over the high topography of  
138 the Alps, indicating an isostatic crustal thickening in response to topography (e.g. Ebbing et al.,  
139 2006). Additionally, we calculate the mass correction for the gravity gradients at a station height

140 of 225 km representing the GOCE satellite altitude. The topographic corrected gravity gradients  
 141 after Bouman et al. (2016) measured by the GOCE ESA satellite mission are presented in the  
 142 appendix.

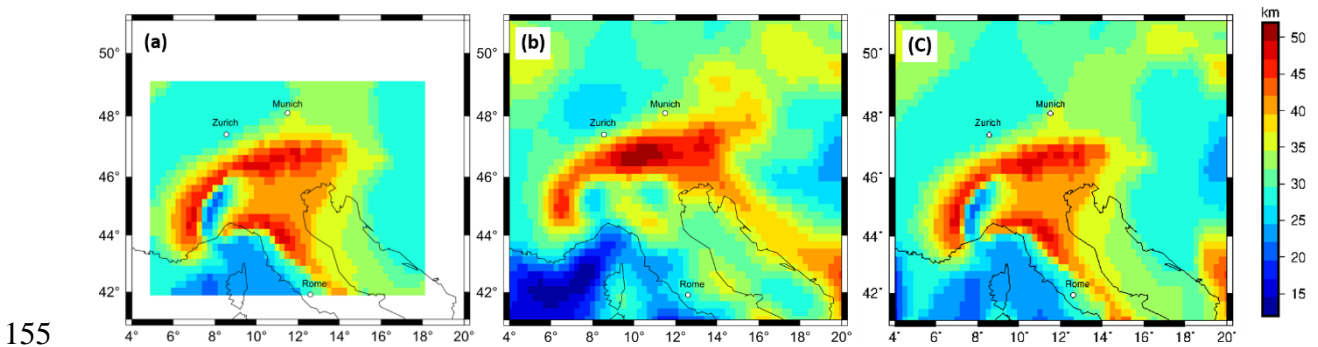
143 For the definition of the slab geometry, we use crustal thickness estimates based on the receiver  
 144 function study by Spada et al. (2013). The crustal thickness map was digitized and the Moho  
 145 gap in the eastern Alps is filled by nearest neighbour interpolation. To avoid edge effects,  
 146 surrounding areas are supplemented by the Moho depth model of the European plate by Grad  
 147 et al. (2009), both data sets were merged using a cosine taper with a taper width of 2° using  
 148 equation (1). The overlapping areas at the grid edges are distance weighted to obtain a smooth  
 149 transition.

$$150 \quad G_{new} = T(x, y) \cdot G_1(x, y) + (1 - T(x, y))G_2 \cdot (x, y) \quad (1)$$

$$152 \quad \text{with: } T(x, y) = \cos \frac{D \cdot \pi}{2 \cdot L}$$

151 *with: G = Grids, T = taper, D = dx, L = Tapper length*

153 The merged Moho depth map is sampled at a regular grid with a cell size of 0.25° (Fig. 2) to be  
 154 consisted with resolution of the topographic and gravity models.



156 *Figure 2 a) digitized Moho depth after Spada et al. (2013) with a 0.25 ° grid spacing, b) Moho depth estimation after Grad et*  
 157 *al. (2009) with a 0.25 ° grid spacing c) Merged Moho depth map from Spada et al. (2016) and Grad et al. (2009) with a grid*  
 158 *resolution of 0.25 ° using a cosine taper with a 2° width.*

159 For the upper mantle seismic velocity, the 3-D shear wave velocity model (MeRE2020) by El-  
 160 Sharkawy et al., (2020) is used (Fig. 3). The model covers the upper mantle across the Alpine-  
 161 Mediterranean area down to a depth of 300 km and absolute shear-wave velocities are given.

162 In this study, relative shear-wave velocities in the depth range from 70 to 200 km are calculated  
163 with respect to a 1-D average shear wave velocity model, the background model is described in  
164 El-Sharkawy et al., (2020). The upper limit of 70 km is introduced because i) we focus on the  
165 contribution of the slab segments removing therefore crustal information from the model ii) the  
166 tomography model MeRE2020 is not sensitive to shallow structures, as a result the slabs are  
167 not well recovered in depths shallower than 70 km iii) we want to ensure a uniform upper  
168 boundary. The lower boundary of 200 km is chosen based on clear images of the Alpine Slab  
169 segments to at least 200 km depth (with exception of the Western Alpine slab), as discussed in  
170 section 1, and the assumptions that depth larger than 200 km will have a negligible effect on  
171 the regional gravity field considered here.

172 The ambient noise tomography by Kästle et al. (2018) is used to define the geometry of the  
173 Western Alpine slab segment, hence we follow the idea of a slab-breakoff in the Western Alps  
174 at 100 km depth (Kästle et al., 2020) as suggested also by Lippitsch et al. (2003) and Beller et  
175 al. (2018). For the eastern Alps, we consider two alternative models. For the first hypothesis,  
176 the P-wave tomography by Lippitsch et al. (2003) is used, to define the Eastern Alpine slab  
177 segment. The second hypothesis is based on Kästle et al. (2020) and El-Sharkawy et al. (2020).  
178 It assumes southward subduction of a short Eurasian Slab as well as northward subduction of a  
179 short Adriatic Slab in the eastern Alps. The slab configurations which are incorporated in the  
180 Alpine density models are discussed in greater detail in section 4.1.

### 181 **3 Conversion of seismic velocities into density distribution**

182 Seismic velocity variations are dependent on temperature and pressure. Densities in the  
183 subsurface are also temperature and pressure dependent. A conversion factor ( $\zeta$ ) can describe  
184 the linear relation between seismic velocities variations and densities variation (e.g. Tiberi et al.  
185 2001; Webb 2009). We convert seismic shear wave velocities from the tomographic model  
186 MeRE2020 by El-Sharawy et al. (2020) in the depth range from 70 to 200 km, as discussed in

187 section 2, to obtain a density distribution of the upper mantle in the Alpine region based on a  
188 conversion factor ( $\zeta$ ). The relationship between seismic velocities and densities is described in  
189 equation (2), this assumption is a strong simplification of reality, but gives a first order  
190 estimation of the expected relative density structure beneath the Alps.

$$191 \quad \rho_{rel} = [Vsv_{abs}(1 + \Delta\%) - Vsv_{abs}] \cdot \zeta = Vsv_{abs} \cdot \Delta\% \cdot \zeta \quad (2)$$

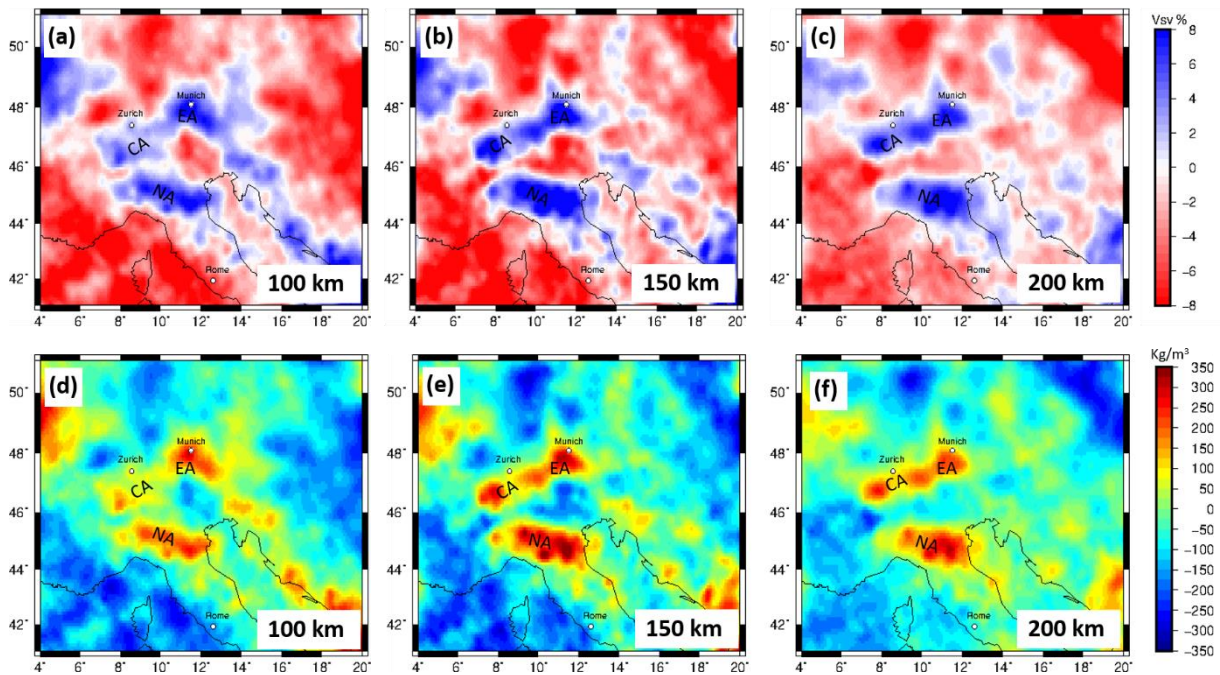
192 *with:  $Vsv_{abs}$  = absolute velocities from MeRE2020;*

193  *$\Delta\%$  = percentage deviation from the MeRE2020 background model;*

194  *$\zeta$  = conversion factor*

195 The result is strongly dependent on the chosen conversion factor. A range for conversion  
196 factors has been proposed in the literature for different rock types ranging from 0.1 to 0.45 (e.g.  
197 Isaac et al., 1989; Isaak, 1992; Karato, 1993; Kogan and McNutt, 1993; Vacher et al., 1998).  
198 The relative shear-wave velocity distribution in a 3D domain from the tomography model  
199 MeRE2020 from El-Sharkawy et al., (2020) is converted using a constant conversion factor ( $\zeta$ )  
200 of 0.3. The converted relative density distribution varies between -240 and 350 kg/m<sup>3</sup>. High  
201 correlations between the structural pattern in the converted density distribution and the relative  
202 seismic velocities are observed (Fig. 3), the similarity in the structure pattern is expected due  
203 to the linear relationship we introduced here. The converted 3D relative density distribution  
204 reflects the variation of seismic velocities in the Alpine lithosphere and therefore includes the  
205 heterogeneities of the subduction slab segments, as seen by the tomographic models (Fig 3).  
206 The relative density model is transferred into tesseroids with a horizontal expansion of 0.2° and  
207 a vertical expansion of 3 km. The Tesseroid model is forward calculated in order to estimate the  
208 gravity response of the converted density distribution of the Alpine lithosphere in the depth  
209 interval of 70 km to 200 km. No horizontal extensions of the mantle model are introduced  
210 because relative densities are used and therefore edge effects are not expected to be significant  
211 and would only affect the outer most degrees of the model. The slab segments are located central  
212 in the model far away from possible artifact due border effects.



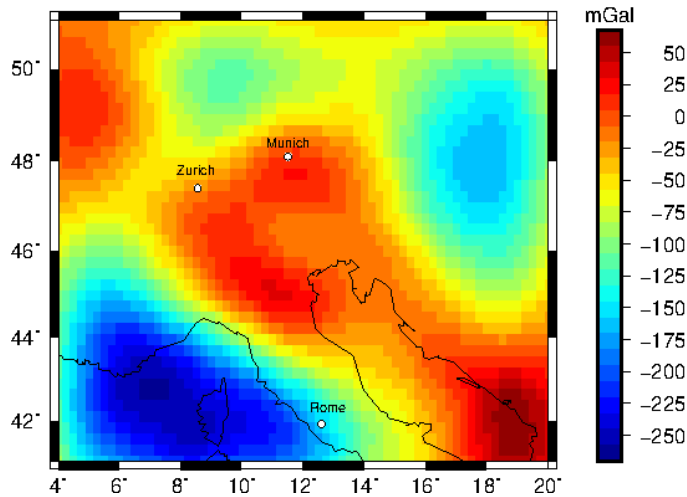


214

215 *Figure 3 (a)-(c) Depth slices of relative surface wave velocities ( $V_{sv}$ ) from MeRE2020 (El-Sharkawy et al., 2020). (d)-(f)*  
 216 *converted relative density distribution in different depths based on a conversion factor ( $\zeta$ ) of 0.3. CA = Central Alpine Slab;*  
 217 *EA = Eastern Alpine Slab; NA = Northern Apennine Slab*

### 218 3.1 Results

219 In the forward calculated gravity field, a gravity high with a magnitude of  $\sim 40$  mGal is observed  
 220 over the Alps (Fig. 4). That might be interpreted as relating to the proposed slab segments in  
 221 the Northern Apennine and Alpine area. However, the gravity field (and gradients, see appendix)  
 222 is dominated by anomalies outside the Alpine realm (Fig. 4), for instance in the Ligurian Sea  
 223 and the Dinaride-Hellenide Orogen. Therefore, in the next step, we try to concentrate on the  
 224 seismic anomalies in the Alpine realm that can be related to the slab segments.



225

226 *Figure 4 Forward calculated gravity signal from relative density distribution converted from relative seismic velocities using*  
 227 *a conversion factor of 0.3 at a station height of 6040m.*

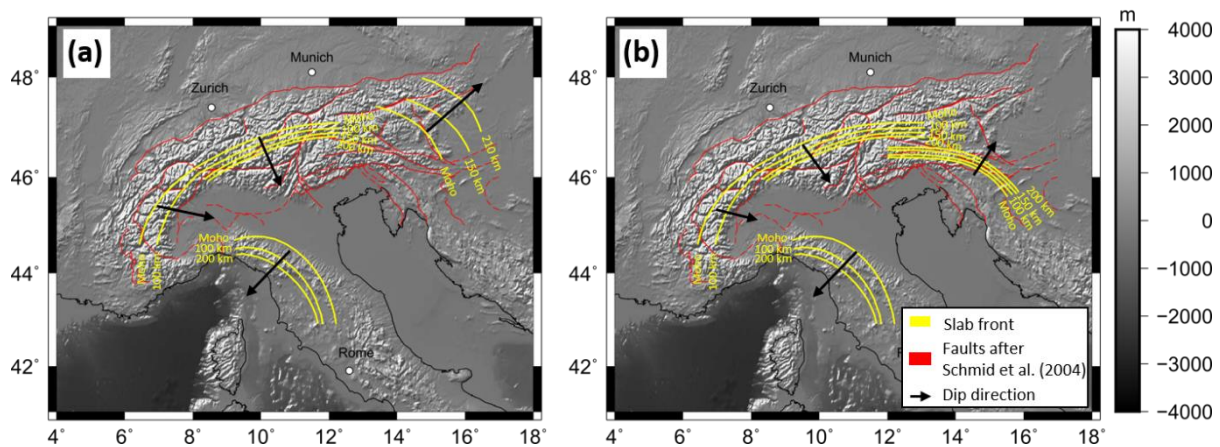
## 228 **4 Slab models**

229 To estimate the gravity contribution of independent slab segments we introduce different  
 230 models for the subducting lithosphere. First, we use a set of models with simple constant density  
 231 distribution in the slab, where the parameters, namely the density contrast and thickness of the  
 232 slab segment is varied (approach 2). Secondly, we create a set of slab models accounting for  
 233 compositional and thermal variations with depth (approach 3). Those models of approach 3 are  
 234 created with the software package LitMod 3D (Fullea et al., 2009) and here the slabs are strictly  
 235 vertical due to software limitations. Slab models created within LitMod will be referred as  
 236 LitMod models in the following. For all non-LitMod models, the gravity and gravity gradients  
 237 are calculated using tesseroids, which are spherical prisms (Uieda et al., 2016).

### 238 **4.1 Slab modelling with constant density contrast and slab thickness**

239 We define two alternative slab configurations based on crustal thickness model by Spada et al.  
 240 (2013) and several different tomographic studies, see detailed description of the slab  
 241 configurations below. At different depths, isolines are picked in the Moho depth map and  
 242 tomographic images, defining the upper boundary of subducting slab segments. The isoline of  
 243 the crust mantle boundary (Moho interface) is used as an onset of the slab to the crust and  
 244 defines the upper boundary of the subduction slab segment. At upper mantle depth, increased

245 seismic velocity anomalies in tomographic models beneath the Alps are interpreted as contrast  
 246 between colder and therefore denser subducting material to the surrounding mantle material. At  
 247 100, 150, and 200 km depth, the upper boundary of the slab segment is defined at the 0%  
 248 contour line of the relative seismic velocity, marking the transition from rocks with low velocity  
 249 to high velocity rocks. The isolines at the Moho interface, 100 km, 150 km and 200 km depth  
 250 are displayed upon the Alpine topography (Fig. 5 a-b) Vertical interpolation between the upper  
 251 boundary isolines at different depths (Moho depth, 100, 150 and 200 km) define a continuous  
 252 surface of the upper slab boundary. The lower boundary of the slabs and therefore the thickness  
 253 of the slab segment is not picked based on seismic data but assumed to have constant  
 254 thicknesses for simplifications. The thickness is varied for different models from 60 to 100 km  
 255 depth.



257 *Figure 5 Defined isolines based on crustal thickness estimations and seismological tomography models for the upper slab*  
 258 *boundary for (a) Configuration 1 and (b) Configuration 2. Black arrows indicate the subduction direction. In red the fault*  
 259 *configuration after Schmid et al. (2004).*

### 260 3.1.1 Alternative slab configurations

261 We define two different slab configurations. Configuration 1 (Fig. 5a) features a northeast  
 262 subducting slab segment in the Eastern Alps based on Lippitsch et al. (2003). A Central Alpine  
 263 slab segment is defined based on Lippitsch et al. (2003) and MeRE2020 (El-Sharkawy et al.,  
 264 2020) subducting in south-southeast direction. The Eastern and Central Alpine slab segments  
 265 are separated by a slab gap and show perpendicular subduction directions. The east-southeast-  
 266 ward subducted slab segment in the Western Alps is defined using the tomographic model of

267 Kästle et al. (2018), supporting the idea of slab break-off at about 100 km depth. Only attached  
268 slab segments are considered, ignoring potential mantle upwelling in the break off zone and  
269 neglecting the potentially remaining detached slab segment in larger depths. In addition, a  
270 southwest-subducting slab segment beneath the northern Apennines is considered down to  
271 about 200 km depth, as imaged by MeRE2020 (El-Sharkawy et al., 2020) because of its  
272 proximity to the western Alps.

273 Configuration 2 (Fig. 5b) considers a slab configuration mainly based on the interpretation of  
274 the MeRE2020 model (Fig. 3) by El-Sharkawy et al. (2020). In the Eastern Alps, both a short  
275 southward subducting Eurasian slab segment as well as a short northward subducting Adriatic  
276 slab are assumed. The Central and Western Alpine slab segments as well as the slab beneath the  
277 northern Apennines are identical to Configuration 1.

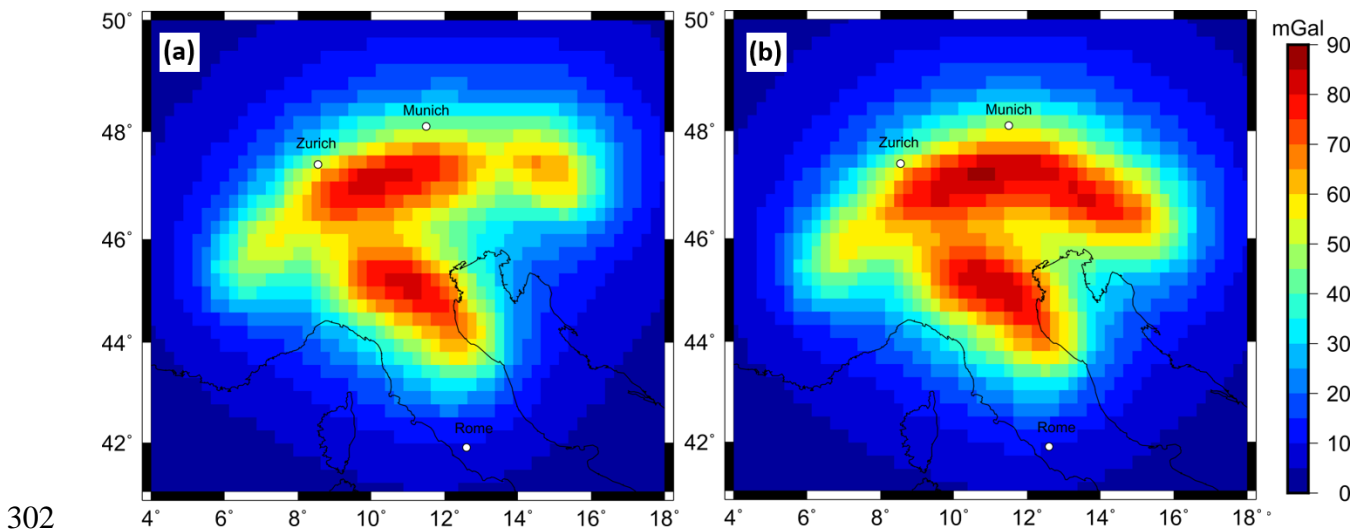
#### 278 4.1.2 Forward calculation

279 To estimate the gravity effect of the slab configurations, the geometries are discretized into  
280 tesseroids with a  $0.2^\circ$  extension in the horizontal domain and a vertical size of 20 km. The  
281 tesseroids range from 40 km to 200 km depth. First, a constant density contrast is assigned to  
282 the entire slab. We test density contrasts from  $20 \text{ kg/m}^3$  to  $80 \text{ kg/m}^3$ . The thickness of the Alpine  
283 slab is not well constrained. We test for three slab volumes by assigning three slab thicknesses,  
284 60 km, 80 km and 100 km based on studies on other subducting slab segments (e.g. Wang et  
285 al., 2020). Due to the curved geometries of the proposed slab segments rectangular tesseroids  
286 with a horizontal expansion of  $0.2^\circ$  will either over- or under-estimate the volume of a  
287 subducting slab at the edges of the slab. The percentage volume share of each tesseroid to the  
288 slab geometry is calculated. The assigned density contrast of the tesseroids which does not lay  
289 fully within the slab geometry is decreased according to the percentage volume within the slab  
290 geometry. Therefore, the density distribution correlates to the hypothetical slab positions and  
291 volumes in the Alpine subsurface without increasing the discretisation resolution of the  
292 tesseroid model beyond the uncertainty of gravity measurements and seismic tomographies.

293 The offset between the 40 km upper tesseroïd boundary to the slab onset at the crust in 44 km  
294 depth is corrected using the same process.

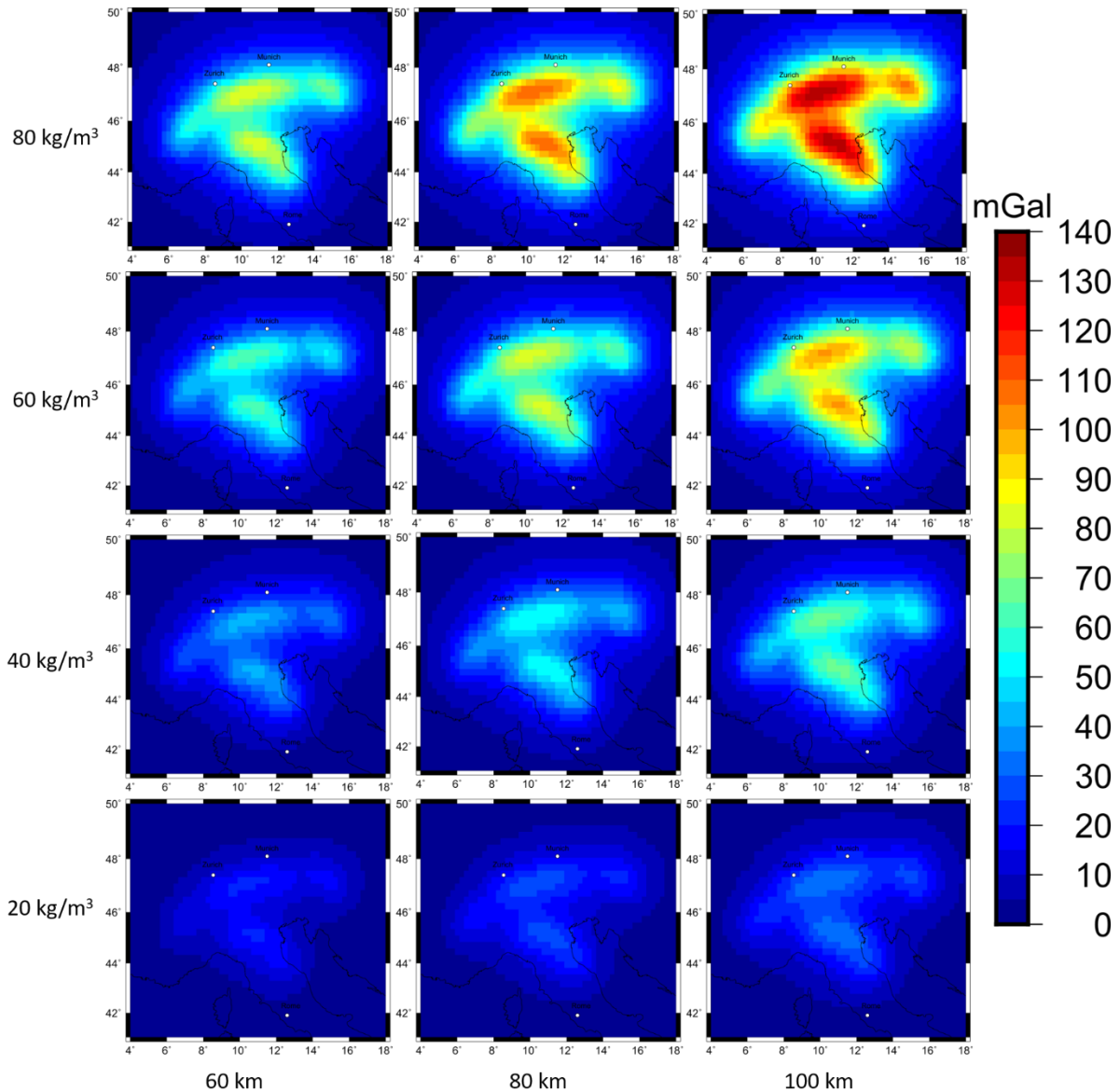
#### 295 4.1.3 Results

296 Forward calculated slab models for predefined slab geometries of Configuration 1 and 2 with a  
297 constant density contrast of  $60 \text{ kg/m}^3$  and a constant thickness of 80 km result in a sharp gravity  
298 signal ranging from 70 mGal to 100 mGal (Fig. 6). Both models generate gravity signals in the  
299 order of magnitude of 70 mGal in the Central Alpine region as well as in the Apennine. The  
300 gravity signal in the Eastern Alps differ for the two hypotheses (Fig. 6 a, b). The Western Alpine  
301 slab segment shows the weakest signal in both models.



303 *Figure 6 Forward calculated gravity disturbance signal at a station height of 6040 m for predefined sub-crustal slab geometries*  
304 *with a content density contrast of  $60 \text{ kg/m}^3$  and a constant thickness of 80 km. (a) predefined slab configuration 1 (b) predefined*  
305 *slab configuration 2.*

306 The gravity signal ranges from 30 to 110 mGal depending on the assigned density contrast and  
307 thickness for both slab geometry models (Fig. 7). The highest magnitude of forward calculated  
308 gravity signal is in the order of 110 mGal and is observed for a slab model with a density  
309 contrast of  $80 \text{ kg/m}^3$  and a constant slab thickness of 100 km, while the lowest signal is  
310 produced by a combination of  $20 \text{ kg/m}^3$  density contrast and a slab thickness of 60 km. Similar  
311 gravity response is produced by different combinations of density contrast and volume. The  
312 signal pattern is influenced by the predefined slab geometry, while the magnitude of the gravity  
313 signal is depending on the density contrast and thickness (Fig. 7).



314

315 *Figure 7 Forward calculated gravity disturbance signal for 12 different combination of density contrast and slab thickness for*  
 316 *sub-crustal slab configuration 1 at a station height of 6040 m.*

317 Forward calculated gravity gradients at satellite height show the same dependency of signal  
 318 strength (see Appendix). The forward calculated gravity field of approach 2 differs significantly  
 319 from the forward calculated gravity field of the complete mantle density inhomogeneity of  
 320 approach 1 (Fig. 4), which only reaches a positive mantle effect of maximum 50 mGal.

#### 321 **4.2 Geophysical and petrological modelling with LitMod**

322 For modelling the Alpine slab segments taking temperature and pressure variations as well as  
 323 composition of the lithosphere and sub lithosphere into account, the geophysical and  
 324 petrological modelling software LitMod 3D is utilized (Fullea et al.,2009). LitMod 3-D is a

325 finite difference code, which allows the modelling of lithospheric and sub lithospheric  
 326 structures down to 400 km depth by solving the heat transfer, thermodynamical, rheological,  
 327 geopotential, and isostasy equations (Afonso et al., 2008; Fullea et al., 2010).

328 A LitMod model consists of a set of crustal, lithospheric- and sub lithospheric layers  
 329 characterized by their petrophysical and thermal properties, which are used as input data (Fullea  
 330 et al., 2010). LitMod provides as an output i.e. the density -, temperature-, pressure- distribution  
 331 as well as the forward calculated gravity disturbance and gravity gradients (Fullea et al. 2009).  
 332 The assigned composition for the different layers is calculated using a LitMod subroutine which  
 333 utilizes the Perple\_X algorithm of Connolly (2009). Perple\_X calculates in the LitMod  
 334 implementation the specific bulk rock properties based on the six main lithospheric oxides  
 335 (SiO<sub>2</sub>, Al<sub>2</sub>O<sub>3</sub>, FeO, CaO, Na<sub>2</sub>O) by minimizing Gibbs free energy equation. The Alpine  
 336 lithosphere and sub lithosphere as well as the proposed slab segments are modelled using  
 337 standard global lithospheric and sub lithospheric compositions to test the influence of  
 338 compositional variations within the slab segments on the gravitational signal. Here, we use the  
 339 so-called Tecton and Proterozoic type-composition (Table 1). Those compositions were chosen  
 340 for a model with a homogeneous crust, lithosphere and sub-lithosphere, where the density  
 341 changes as a function of temperature and pressure based on the assigned compositions. The  
 342 different slab composition is introduced to test whether a compositional contrast, in addition to  
 343 the expected thermal difference, results in a significant density contrast between the slab and  
 344 the surrounding material.

345 *Table 1: Mineralogical composition for the lithospheric and sub lithospheric structure.*

| Major Oxide<br>Compositions    | Aver. Tecton<br>Gnt. SCLM <sup>a</sup> | Aver. Tecton<br>Gnt. Peridotite <sup>a</sup> | Average Proterozoic<br>Massif | PUM <sup>b</sup> | DMM <sup>c</sup> |
|--------------------------------|--|--|-------------------------------|------------------|------------------|
| SiO <sub>2</sub>               | 44.5                                   | 45   | 45.2                          | 45               | 44.7             |
| Al <sub>2</sub> O <sub>3</sub> | 3.5                                    | 3.9  | 2                             | 4.5              | 3.98             |
| FeO                            | 8                                      | 8.1  | 7.9                           | 8.1              | 8.1              |

|                   |      |      |      |      |      |
|-------------------|------|------|------|------|------|
| MgO               | 39.8 | 38.7 | 41.6 | 37.8 | 37.8 |
| CaO               | 3.1  | 3.2  | 1.9  | 3.6  | 3.17 |
| Na <sub>2</sub> O | 0.26 | 0.24 | 0.13 | 0.36 | 0.13 |

346 <sup>a</sup> Classifications according to Griffin et al. (1999b), <sup>b</sup> McDonough & Sun (1995), <sup>c</sup> Workman & Hart (2005) DMM = Depleted  
347 mid-oceanic ridge basalt mantle, PUM = primitive upper mantle.

348 First, we create a reference model ( $M_0$ ) without a slab segment. This model contains topography  
349 from the ETOPO1 dataset (Amante and Eakins, 2009), the Moho depth from Spada et al. (2013)  
350 and Grad et al. (2009). The lithosphere asthenosphere boundary (LAB) is a required interface  
351 for the LitMod 3D to divide the model between the lithosphere and sub lithosphere and to assign  
352 compositions. We introduce a fixed technical LAB at a depth of 100 km throughout the model  
353 despite of the presence of slabs as the LAB is defined as the 1300°C isotherm. This set-up avoids  
354 that the isotherm follows the geometrical shape of the slab, which would lead to a location in  
355 unrealistic large depths (>200 km). In addition, we neglect the topography of the LAB for  
356 several reasons: i) the information of the lithospheric thickness in the Alpine forelands is spare  
357 and under ongoing discussions, ii) the fixed depth value is based on thermal isostasy LAB  
358 estimations from Artemieva et al. (2019), which shows a LAB depth in the range of 80 to 120  
359 km depth in the Alpine forelands. This technical LAB is used to parameterize the model and is  
360 not meant to represent the topography of the LAB. The modelled slab segments are extending  
361 vertically downwards.

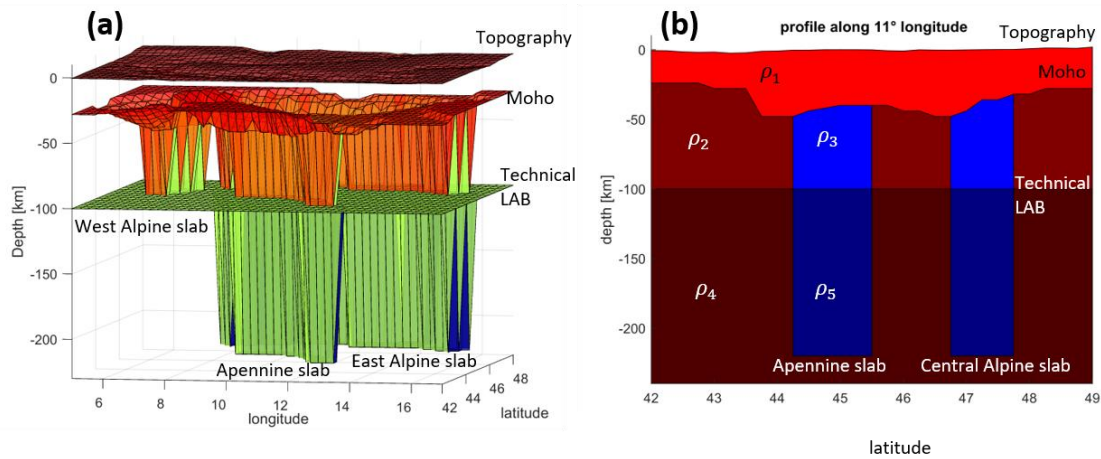
362 Slab segments are introduced stepwise for the lithosphere and sub lithosphere domains into the  
363 model as well as thermal anomalies for the slab segment beneath the technical LAB, which  
364 describes the 1300°C isotherm (Table 2). Calculating the difference to the reference model ( $M_0$ )  
365 allows to estimate the effect a slab segments has on the density, temperature distribution of the  
366 Alpine subsurface and therefore on the Alpine gravity field based on slab position, slab  
367 geometry and composition.



368 *Table 2: Different LitMod models and there incorporated lithospheric and sub lithospheric structures and compositions.*

| <b>Models</b>        | <b>Slab geometries</b> | <b>Slab composition (mantle)</b> | <b>Mantle composition</b> | <b>Slab composition (sub lithosphere)</b> | <b>Sub lithosphere composition</b> | <b>Thermal anomaly within sub lithospheric slab</b> |
|----------------------|------------------------|----------------------------------|---------------------------|---|------------------------------------|---|
| <b>M<sub>0</sub></b> | -                      | -                                | aver. Tecton Gnt.         | -   | PUM                                | -   |
| <b>M<sub>1</sub></b> | Configuration 1        | Aver. Tecton Gnt. Peridotite     | aver. Tecton Gnt.         | -   | PUM                                | -   |
| <b>M<sub>2</sub></b> | Configuration 2        | Aver. Tecton Gnt. Peridotite     | aver. Tecton Gnt.         | -   | PUM                                | -   |
| <b>M<sub>3</sub></b> | Configuration 1        | Aver. Tecton Gnt. Peridotite     | aver. Tecton Gnt.         | DMM                                       | PUM                                | -100 °K   |
| <b>M<sub>4</sub></b> | Configuration 2        | Aver. Tecton Gnt. Peridotite     | aver. Tecton Gnt.         | DMM                                       | PUM                                | -100 °K   |
| <b>M<sub>5</sub></b> | Configuration 1        | Aver. Tecton Gnt. Peridotite     | aver. Tecton Gnt.         | PUM                                       | PUM                                | -   |
| <b>M<sub>6</sub></b> | Configuration 1        | Aver. Tecton Gnt. Peridotite     | aver. Tecton Gnt.         | DMM                                       | PUM                                | -   |
| <b>M<sub>7</sub></b> | Configuration 1        | Aver. Tecton Gnt. Peridotite     | aver. Tecton Gnt.         | DMM                                       | PUM                                | -200 °K   |
| <b>M<sub>8</sub></b> | Configuration 2        | Average Proterozoic Massif       | aver. Tecton Gnt.         | -   | PUM                                | -   |

369 A positive density contrast between subducting material and the surrounding mantle material  
370 results in a negative buoyancy force. A density contrast is introduced into the LitMod model by  
371 a difference in composition between the subducting denser slab and the surrounding mantle  
372 (Fig. 9). Here, we use Tecton like compositions for the lithosphere and the subducting slab  
373 segments since the Alpine slab segments result from continent-continent collision (Tables 1 and  
374 2). A later model features a Proterozoic slab composition (M<sub>8</sub>). Depleted mid-oceanic ridge  
375 basalt mantle (DMM) and primitive upper mantle (PUM) are used for the sub lithospheric  
376 domain. Additional to the density contrast within the sub lithosphere, a temperature anomaly of  
377 – 100 K is introduced for the sub lithospheric part. Later models include a variation of  
378 temperature anomalies (M<sub>5</sub>, M<sub>6</sub>, M<sub>7</sub>). Note those compositions are used as a first order test and  
379 serve as a starting point for synthetic slab models to illustrate the compositional and thermal  
380 effect on the gravity signal by influencing the density distribution. They do not necessary  
381 represent the compositional mantle environment in the Alpine region.



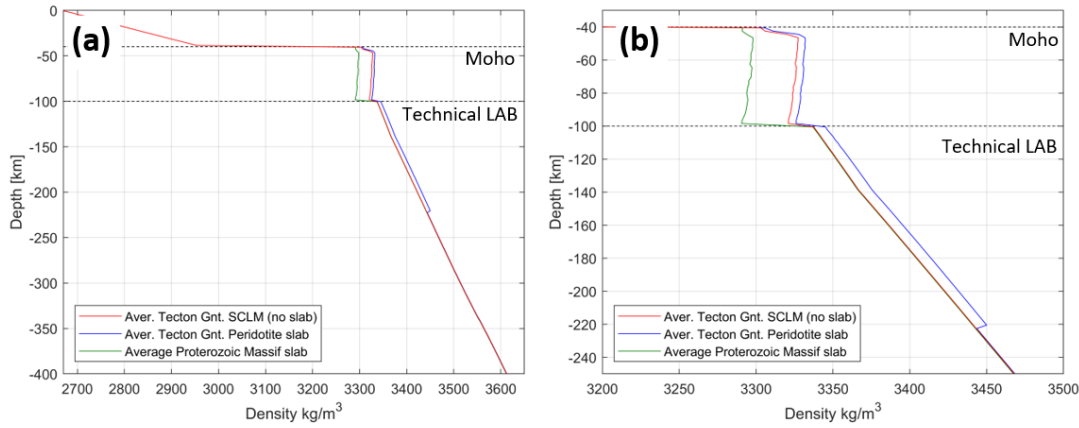
382

383 *Figure 8 (a) 3D model set up using LitMod 3D. Topography, Moho and LAB depth as well as the vertical incorporated slab*  
 384 *models are used as input layers with assigned petrophysical and thermal properties. (b) Profile along 11° longitude through a*  
 385 *LitMod model containing Topography, crustal and lithospheric thickness as well as a slab segment.  $\rho_{0-5}$  indicate*  
 386 *petrophysical and thermal property variations for each layer.*

#### 387 4.2.1 Results

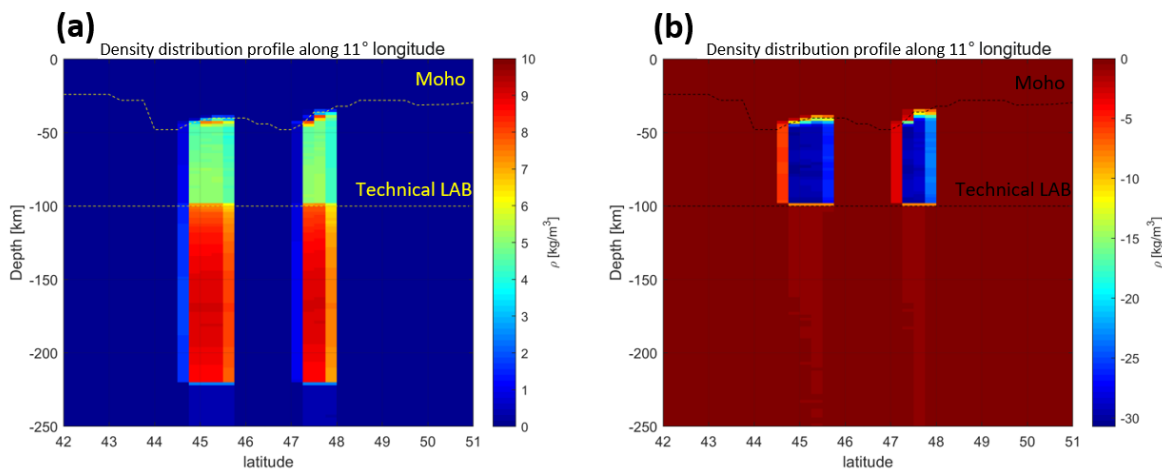
388 The gravity signal of the predefined slab segments is forward calculated as well as the  
 389 background model without incorporation of slab segments. The residual between both forward  
 390 calculations gives the gravitational contribution of the slab segments, while other gravitational  
 391 effects, like the topography or crustal thickness variation and mantle variations outside the slab  
 392 are not considered.

393 A slab segment with an average Tecton Gnt. composition ( $M_1$ ,  $M_2$ ) results in a slightly denser  
 394 material compared to the surrounding mantle ( $M_0$ ), while a slab segment with a Proterozoic  
 395 composition ( $M_8$ ) shows a less dense lithospheric structure compared to the reference model  
 396 ( $M_0$ ), this composition results in less dense slab segment, which would not be subducted due to  
 397 the positive buoyancy (Fig. 10). However, we aim to illustrate the effect composition has on  
 398 the density distribution within the slab and to the surrounding mantle and show the importance  
 399 of correct compositional information, therefore we focus on the difference in density contrast  
 400 between slab and surrounding mantle and neglecting the sign of the density contrast.



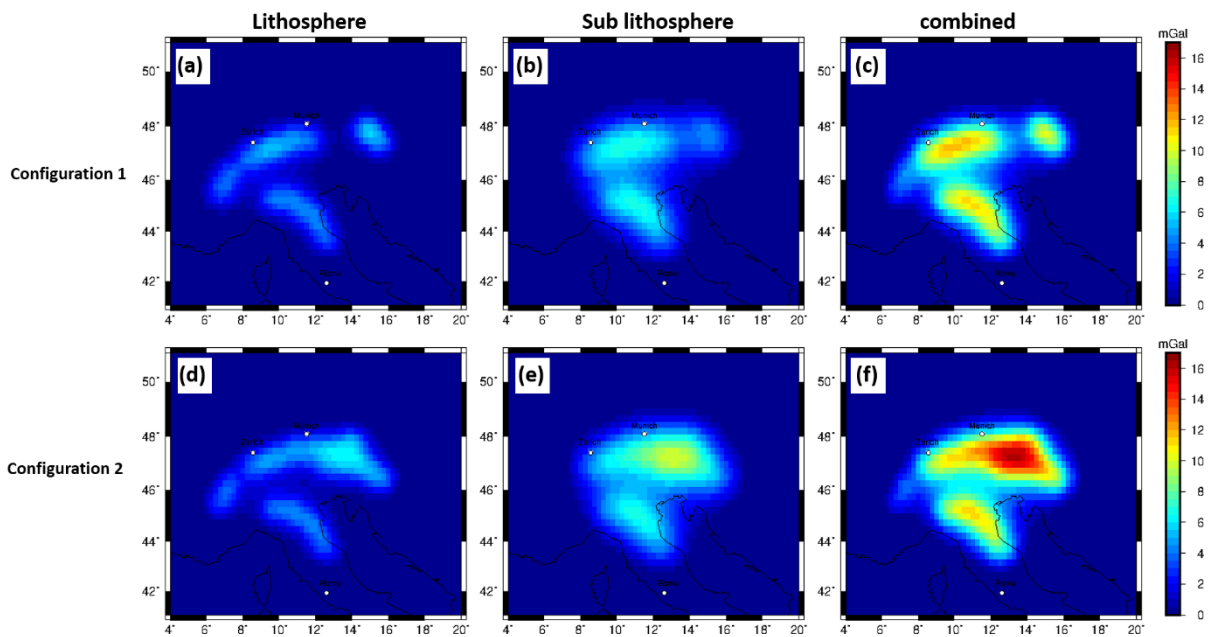
401  
 402 *Figure 9 (a) density profile at 11° longitude and 45° latitude for the full vertical model space of 400 km depth. Density profiles*  
 403 *for 3 different models ( $M_0$ ,  $M_1$ ,  $M_9$ ) with different compositional properties are shown. (b) Zoomed in profile at the depth range*  
 404 *of present slab segments.*

405 The difference in density distribution (density contrast) within the slab segments with a Tecton  
 406 composition ( $M_1$ ,  $M_3$ ) to the reference model ( $M_0$ ) is in the order of  $5 \text{ kg/m}^3$  for the lithosphere  
 407 and in the order of  $10 \text{ kg/m}^3$  for the sub lithospheric domain (Fig. 10a). The density variations  
 408 within the lithospheric and sub lithospheric slab domain are less than  $1 \text{ kg/m}^3$  resulting from  
 409 both depth dependent variations in pressure and temperature. Between lithosphere and sub  
 410 lithosphere, a rapid increase in density contrast is observed (Fig. 10a). The density contrast of  
 411 a lithospheric Proterozoic slab composition ( $M_9$ ) to the reference model ( $M_0$ ) is in the order of  
 412  $-30 \text{ kg/m}^3$  (Fig. 10b).



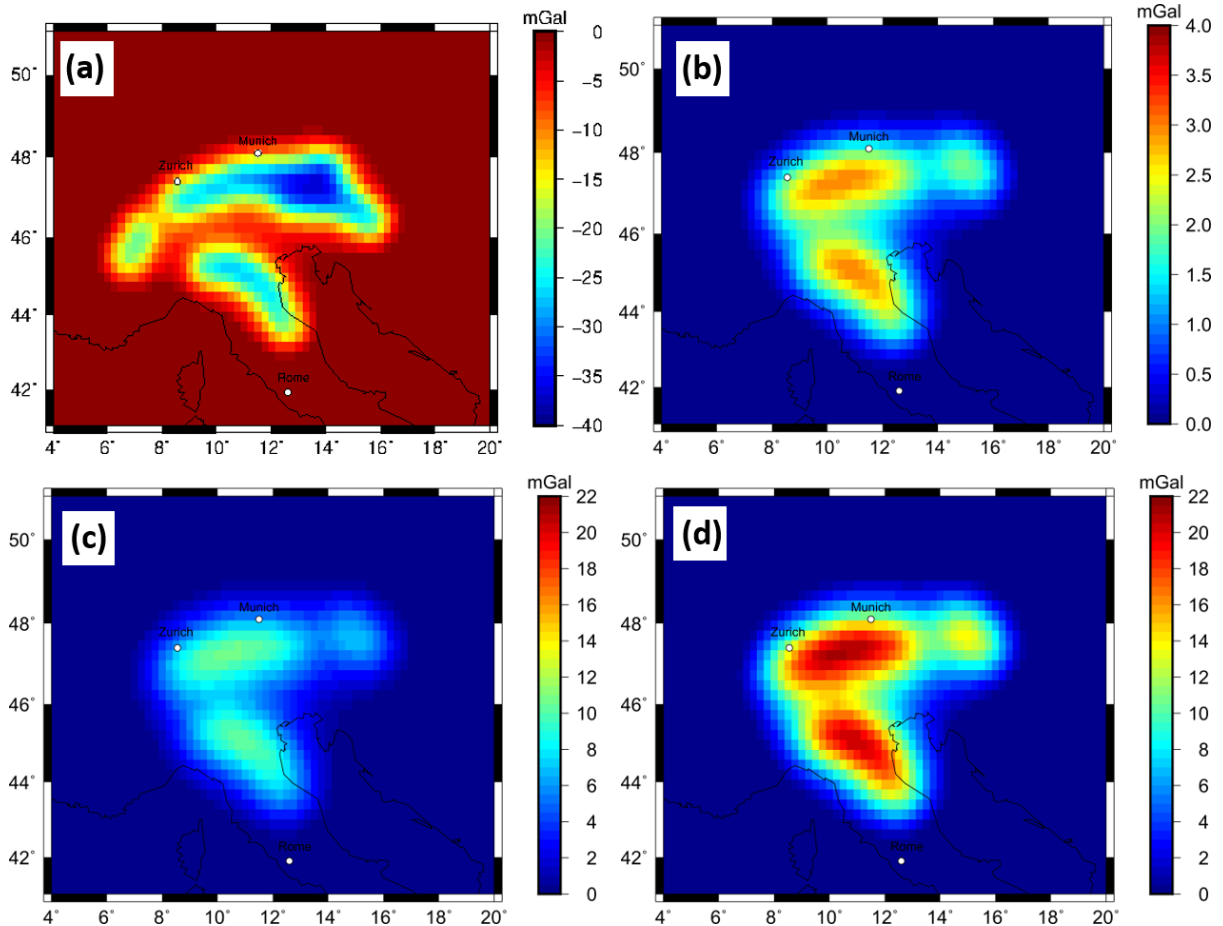
413  
 414 *Figure 10 (a) residual density contrast for lithospheric and sub lithospheric slab segments of model ( $M_3$ ) with Tecton like*  
 415 *composition within the lithosphere and PUM and DMM composition in the sub lithosphere with an additional thermal anomaly*  
 416 *of  $-100^\circ \text{ k}$  for the sub lithospheric slab segment to the background model ( $M_0$ ). (b) Residual lithospheric density contrast of a*  
 417 *Proterozoic lithospheric slab segment ( $M_8$ ) to a Tecton compositional surrounding mantle ( $M_0$ ). Residual density contrast is*  
 418 *limited to the technical LAB as the sub-lithospheric part is identical to the reference model (see also Fig. 9b)*

419 The gravity signal caused by the proposed slab segment configurations is estimated for  
 420 lithosphere and sub lithosphere separately. The forward calculated gravity effect, at topographic  
 421 surface level, for the slab configuration 1 for the lithospheric part is in the order of 4 mGal  
 422 while the sub lithospheric gravity signal is in the range of 7 mGal (Fig. 12a, b). The combined  
 423 gravity signal is in the order of 12 mGal (Fig. 12c). The gravity signal in the Eastern Alps for  
 424 Configuration 2 is significantly larger in the order of 17 mGal for the combined model (Fig.  
 425 12f).



426  
 427 *Figure 11 Residual of the forward calculated  $g_z$  gravity signal of lithospheric slabs at surface station height based on LitMod*  
 428 *models with Tecton like compositions in the lithosphere and PUM and DMM compositions in the sub lithosphere ( $M_1$ ,  $M_2$ ,  $M_3$ ,*  
 429  *$M_4$ ) with an additional thermal anomaly of  $-100^\circ$  k for the sub lithospheric slab segment, for predefined slab Configuration to*  
 430 *the background model ( $M_0$ ). (a)-(c) Configuration 1. (d)-(f) Configuration 2. Crustal and topographic contribution are nullified.*

431 The calculated gravitational effect of a slab segment with Proterozoic composition and a Tecton  
 432 surrounding mantle composition is in the order of -40 mGal for the  $g_z$  component (Fig. 12 a).



433

434 *Figure 12 (a) Forward calculated gravity effect of a Proterozoic lithospheric slab segment to a Tecton compositional*  
 435 *surrounding mantle for configuration 2, obtained by calculating the residual between  $M_8$  and  $M_0$ . (b) gravity signal produced*  
 436 *by purely compositional effect in the sub lithosphere between a PUM and DMM composition, obtained by calculating the*  
 437 *residual between  $M_5$  and  $M_6$ . (c) gravity signal produced by purely thermal anomaly of  $-100^\circ\text{K}$  for a sub lithospheric slab*  
 438 *segment, obtain by calculating the residual between  $M_3$  and  $M_6$ . (d) gravity signal produced by purely thermal anomaly of*  
 439  *$-200^\circ\text{K}$  for a sub lithospheric slab segment obtained by calculating the residual between  $M_6$  and  $M_7$ .*

440 The gravity response to a compositional variation within the sub lithosphere between the  
 441 incorporated slab segment (DMM composition) and the surrounding mantle (PUM composition)  
 442 is in the order of 4 mGal (Fig. 12b). The gravity response for a pure thermal anomaly of -100  
 443 K within the sub lithospheric slab segment is in the order of 16 mGal (Fig. 12c), while a pure  
 444 thermal anomaly of -200 K within the sub lithospheric slab segment is in the order of 21 mGal.

## 445 5 Discussion

446 The imprint of the gravity response caused by the density distribution based on direct  
 447 conversion of seismic velocities (approach 1) is visible, however, individual and independent  
 448 slab segments cannot be identified (Fig. 4). The strength of this approach is that it is fast to

449 implement and can provide a first order characterization of the gravity signal and slab  
450 geometries of subducting lithosphere. However, a clear characterization of subducting slab  
451 segments is not possible. First of all, the density model depends on the resolution and  
452 regularization of the seismological model, which can lead to distortions in the gravity response  
453 (e.g. Root, 2020). The method is dependent on the choice of the conversion factor and might  
454 overestimate the density (see the large negative anomaly in the Ligurian Sea). The conversion  
455 factor is a strong simplification of nature and for such a geodynamic complex area, a constant  
456 conversion factor is not adequate.

457 The forward calculated gravity field with competing predefined slab geometries (approach 2)  
458 shows a clear gravity signal, where the individual slab segments are distinguishable (Fig. 6).

459 A relative gravity low related to the slab gap in the Eastern Alps is a prominent feature in the  
460 gravity signal of Configuration 1 (Fig. 6a). The eastern Alpine slab segment of Configuration  
461 1, due to its relatively small volume, result in a lower signal compared to the Central Alpine  
462 slab segment.

463 Configuration 2 shows a larger gravity signal in the Eastern Alps up to 100 mGal (Fig. 6b)  
464 compared to Configuration 1. The increase of the gravity signal is attributed to the subduction  
465 of both Eurasian and Adriatic lithosphere in the Eastern Alps. The gravity signal shows a  
466 continuous transition from the Central Alps to the Eastern Alps, where the contribution of the  
467 destined slab segment cannot be distinguished in the resulting gravity field (Fig. 6b). In the  
468 Western Alps, Configuration 1 and 2 show a lower gravity signal compared to the Central Alps.  
469 This is attributed to the much shallower Western Alpine slab segment that penetrate down to  
470 100 km depth.

471 The gravity signal is influenced by both the assigned density contrast and thickness of the slab.  
472 A trade of between both parameters is clearly observable as the same gravity response of the  
473 slab configuration can be achieved with different values of density contrast and slab thickness.

474 Therefore, making it impossible to derive slab properties in form of density contrast and slab  
475 thickness from the gravity field (Fig. 7).

476 The calculated densities in LitMod 3-D models (approach 3) are estimated taking temperature  
477 and pressure variations into account based on an assigned composition. The composition has a  
478 strong influence on the resulting density contrast. In the case that the compositional contrast  
479 between slab segment and surrounding mantle is small, the density contrast is consequently  
480 small as well (Fig. 9 and 10a). With increasing compositional differences, the density contrast  
481 increases as well. A strong density contrast within the slab segment is recognizable between  
482 lithospheric and sub lithospheric domain (Fig. 10a and b), while the variations between the slab  
483 and surrounding mantle remain small.

484 The gravity signal shows in the Eastern Alps significant larger signal from the lithosphere and  
485 sub lithosphere domain for Configuration 2 (Fig. 11d, e, and f) compared to Configuration 1  
486 (Fig. 11a- c). The different slab segments are distinguishable with the exception of the two slab  
487 segments in the Eastern Alps in Configuration 2 (Fig. 11). The contribution from the  
488 lithospheric domain to the gravity signal is smaller than from the sub lithospheric domain (Fig.  
489 11b, and e). However, the slab gap and the eastern slab segment feature can be recognized in  
490 the lithospheric part in Configuration 1 but not in the gravity signal of the full model.

491 The Proterozoic slab segment has a larger gravity response compared to the Tecton-like  
492 composition. This gravitational signal is negative due to the less dense Proterozoic composition  
493 in comparison to the reference model ( $M_0$ ) (Fig. 12a).

494 Sub lithospheric composition has only a small influence on the gravity field, in the order of 4  
495 mGal (Fig. 12b). However, a thermal anomaly within the sub lithospheric slab in the order of -  
496 100K result in a gravitational response of 16 mGal (Fig. 12c) and for a -200 K anomaly in the  
497 order of 21 mGal (Fig. 12d). Both the composition and the thermal variation influence the  
498 density and consequently the gravity response. However, the thermal component is a much  
499 larger contributor.

500 For the three approaches (section 3, 4.1 and 4.2) a measurable gravity effect of the subducting  
501 slab segments is observable. The independent slab segments are distinguishable to a certain  
502 degree with the exception of the bivergent slab configuration in the Eastern Alps (Fig. 6, and  
503 11) and the model containing converted density from seismic velocities (Fig 4), while the slab  
504 configurations cannot be separated at satellite altitude (Appendix). Forward calculated gravity  
505 anomalies from converted density distribution suggest a gravitational signal of the slab  
506 segments in the order of 40 mGal which corresponds to a density contrast of 20 to 40 kg/m<sup>3</sup> in  
507 the models with predefined slab geometry. The models with a Tecton like composition suggest  
508 a gravity effect of the slab segments in the order of only 16 mGal, corresponding to a density  
509 contrast of 20 kg/m<sup>3</sup> in the simple model. Increasing the compositional difference with a Tecton  
510 composition suggests a gravity signal in order of 30 mGal and is in line with the converted  
511 density model.

512 All three methods show a positive gravity signal contribution, which can be related to sub-  
513 crustal density variations for approach 1 and to predefined sub-crustal slab segments for  
514 approach 2 & 3, up to 40 mGal to the Alpine gravity field. That is significant in comparison to  
515 the observed Bouguer Anomaly with a minimum of ~-200 mGal. If this contribution is not  
516 considered, a significant part of the gravity signal is attributed to crustal thickness or intra-  
517 crustal sources. Due to the long-wavelength appearance of the gravity effect, that might not be  
518 relevant for small-scale or local studies, the effect is only seen as a shift. For gravity models of  
519 larger areas (e.g. Eastern Alps) or even the entire regions that should not be neglected. For one,  
520 estimates of crustal thickness or the mass distribution are significantly biased, and placing the  
521 Alps in the geodynamic context of the surrounding requires a careful and complete  
522 consideration of all sources in order to provide realistic density distribution required for  
523 geodynamic models (e.g. Reuber et al., 2019).

## 524 **6 Conclusions**



525 We have addressed the potential gravity effect of proposed slab segments in the Alpine region  
526 using three different modelling approaches.

527 • Converted density from seismic tomography: In the resulting gravity signal the imprint  
528 of slab segments is visible, however, distinguishing between the different and  
529 independent slab segments is not possible.

530 • Models with predefined slab segments are dependent on the assigned density contrast  
531 and volume as well as on the predefined positions of the slab segments. The gravity  
532 signal caused by the slab segments are sharp and can be separated for the different slab  
533 segments for the gravity field at the surface. Significant gravity contributions from slab  
534 segments below 200 – 250 km to the Alpine gravity are unlikely.

535 • Combined petrophysical-geophysical modelling results in the most complex models.  
536 The calculated density variation within the slab is rather small compared to the density  
537 contrast between lithosphere and sub lithosphere. The density distribution within the  
538 slabs, and consequently the gravity field, is highly influenced by the slab composition  
539 and thermal structure.

540 Sub-crustal density variation (approach 1) and predefined slab segments (approach 2 & 3)  
541 suggest a positive sub-crustal gravity contribution of up to 40 mGal. Even though this might be  
542 considered as a maximum gravity estimation of slabs, this value is significant, even compared  
543 to the observed Bouguer Anomaly low of -200 mGal along the Alps. The interpretation of  
544 density variation in the mantle in terms of subducting slab structures is a means to provide a  
545 meaningful representation of the geodynamic complex Alpine area. For future studies correct  
546 slab density structure are crucial to provide a representation of the Alpine geodynamic setting.  
547 Precise estimations of the slab density structure require a correct crustal density and crustal  
548 thickness model. With the integration of further observables, it might be possible to judge on  
549 the correct slab configuration beneath the Alps. Furthermore, future studies based on the

550 AlpArray Network will be of high interest in better defining slab geometries as well as their  
551 properties.

## 552 **Competing interests**

553 The authors declare that they have no conflict of interest.

## 554 **Author contributions**

555 ML carried out the gravity modelling, visualized and interpreted the results and prepared the  
556 first manuscript draft. JE supervised the gravity modelling and interpretation, designed the  
557 original research project, acquisition of the financial support for the project leading to this  
558 publication and writing (reviewing and editing). TM defined the slab configurations based on  
559 tectonic and seismological knowledge and writing (reviewing and editing). AE created and  
560 provided the surface wave tomography model MeRE2020 and writing (reviewing and editing).

## 561 **Acknowledgment**

562 The authors thank the reviewers, Carla Braitenberg and an anonymous referee for their valuable  
563 suggestions, which helped to improve the manuscript significantly.

564 This study is part of the projects "Integrierte 3D Modellierung des Schwere- und  
565 Temperaturfelds zum Verständnis von Rheologie und Deformation der Alpen und ihrer  
566 Vorlandbecken - INTEGRATE" and "Surface Wavefield Tomography of the Alpine Region to  
567 Constrain Slab Geometries, Lithospheric Deformation and Asthenospheric Flow in the Alpine  
568 Region" funded by German Research Foundation (DFG) in the SPP Mountain Building  
569 Processes in 4D.

570 We thank the developer of open scientific Software which were utilized in this study: tesseroids  
571 (Uieda et al., 2016), LitMod 3D (Fullea et al., 2009 and Afonso et al., 2008) and Generic  
572 Mapping Tools (GMT) (Wessel et al., 2013; Wessel & Luis, 2017).

573 **References**

- 574 Afonso, J. C., Fernandez, M., Ranalli, G., Griffin, W. L., & Connolly, J. A. D. (2008). Integrated  
575 geophysical-petrological modeling of the lithosphere and sublithospheric upper mantle:  
576 Methodology and applications. *Geochemistry, Geophysics, Geosystems*, 9(5).  
577
- 578 Amante, C., & Eakins, B. W. (2009). ETOPO1 arc-minute global relief model: procedures, data  
579 sources and analysis.  
580
- 581 Artemieva, I. M. (2019). Lithosphere structure in Europe from thermal isostasy. *Earth-Science*  
582 *Reviews*, 188, 454-468.  
583
- 584 Babuška, V., Plomerova, J., & Granet, M. (1990). The deep lithosphere in the Alps: a model  
585 inferred from P residuals. *Tectonophysics*, 176(1-2), 137-165.  
586
- 587 Beller, S., Monteiller, V., Operto, S., Nolet, G., Paul, A., & Zhao, L. (2018). Lithospheric  
588 architecture of the South-Western Alps revealed by multiparameter teleseismic full-waveform  
589 inversion. *Geophysical Journal International*, 212(2), 1369-1388.  
590
- 591 Bouman, J., Ebbing, J., Fuchs, M., Sebera, J., Lieb, V., Szwillus, W., ... & Novak, P. (2016).  
592 Satellite gravity gradient grids for geophysics. *Scientific reports*, 6(1), 1-11.  
593
- 594 Braitenberg, C. (2015). Exploration of tectonic structures with GOCE in Africa and across-  
595 continents. *International Journal of Applied Earth Observation and Geoinformation*, 35, 88-95.  
596
- 597 Channell, J. E. T., & Horvath, F. (1976). The African/Adriatic promontory as a  
598 palaeogeographical premise for Alpine orogeny and plate movements in the Carpatho-Balkan  
599 region. *Tectonophysics*, 35(1-3), 71-101.  
600
- 601 Connolly, J. A. D. (2009). The geodynamic equation of state: what and how. *Geochemistry,*  
602 *Geophysics, Geosystems*, 10(10).  
603
- 604 Dewey, J. F., Helman, M. L., Knott, S. D., Turco, E., & Hutton, D. H. W. (1989). Kinematics  
605 of the western Mediterranean. Geological Society, London, Special Publications, 45(1), 265-283.  
606
- 607 Ebbing, J., Braitenberg, C., & Götze, H. J. (2001). Forward and inverse modelling of gravity  
608 revealing insight into crustal structures of the Eastern Alps. *Tectonophysics*, 337(3-4), 191-208.  
609
- 610 Ebbing, J., Braitenberg, C., & Götze, H. J. (2006). The lithospheric density structure of the  
611 Eastern Alps. *Tectonophysics*, 414(1-4), 145-155.  
612
- 613 El-Sharkawy, A., Meier, T., Lebedev, S., Behrmann, J., Hamada, M., Cristiano, L., ... & Köhn,  
614 D. (2020). The Slab Puzzle of the Alpine - Mediterranean Region: Insights from a new, High -  
615 Resolution, Shear - Wave Velocity Model of the Upper Mantle. *Geochemistry, Geophysics,*  
616 *Geosystems*, e2020GC008993.  
617
- 618 Fichtner, A., van Herwaarden, D. P., Afanasiev, M., Simutè, S., Krischer, L., Çubuk-Sabuncu,  
619 Y., ... & Trampert, J. (2018). The collaborative seismic earth model: Generation 1. *Geophysical*  
620 *research letters*, 45(9), 4007-4016.  
621

622 Frisch, W. (1979). Tectonic progradation and plate tectonic evolution of the Alps.  
623 *Tectonophysics*, 60(3-4), 121-139.  
624

625 Fullea, J., Afonso, J. C., Connolly, J. A. D., Fernandez, M., García-Castellanos, D., & Zeyen,  
626 H. (2009). LitMod3D: An interactive 3-D software to model the thermal, compositional,  
627 density, seismological, and rheological structure of the lithosphere and sublithospheric upper  
628 mantle. *Geochemistry, Geophysics, Geosystems*, 10(8).  
629

630 Fullea, J., Fernández, M., Afonso, J. C., Vergés, J., & Zeyen, H. (2010). The structure and  
631 evolution of the lithosphere–asthenosphere boundary beneath the Atlantic–Mediterranean  
632 Transition Region. *Lithos*, 120(1-2), 74-95.  
633

634 Ganguly, J., Freed, A. M., & Saxena, S. K. (2009). Density profiles of oceanic slabs and  
635 surrounding mantle: Integrated thermodynamic and thermal modeling, and implications for the  
636 fate of slabs at the 660 km discontinuity. *Physics of the Earth and Planetary Interiors*, 172(3-4),  
637 257-267.  
638

639 Götze, H. J., Lahmeyer, B., Schmidt, S., & Strunk, S. (1994). The lithospheric structure of the  
640 Central Andes (20–26 S) as inferred from interpretation of regional gravity. In *Tectonics of the*  
641 *southern Central Andes* (pp. 7-21). Springer, Berlin, Heidelberg.  
642

643 Götze, H. J., & Krause, S. (2002). The Central Andean gravity high, a relic of an old subduction  
644 complex?. *Journal of South American Earth Sciences*, 14(8), 799-811.  
645

646 Götze, H. J., & Pail, R. (2018). Insights from recent gravity satellite missions in the density  
647 structure of continental margins—With focus on the passive margins of the South  
648 Atlantic. *Gondwana Research*, 53, 285-308.  
649

650 Grad, M., Tiira, T., & ESC Working Group. (2009). The Moho depth map of the European  
651 Plate. *Geophysical Journal International*, 176(1), 279-292.  
652

653 Griffin, W. L., O'reilly, S. Y., Afonso, J. C., & Begg, G. C. (2009). The composition and  
654 evolution of lithospheric mantle: a re-evaluation and its tectonic implications. *Journal of*  
655 *Petrology*, 50(7), 1185-1204.  
656

657 Gutknecht, B. D., Götze, H. J., Jahr, T., Jentzsch, G., & Mahatsente, R. (2014). Structure and  
658 state of stress of the Chilean subduction zone from terrestrial and satellite-derived gravity and  
659 gravity gradient data. *Surveys in Geophysics*, 35(6), 1417-1440.  
660

661 Handy, M. R., Schmid, S. M., Bousquet, R., Kissling, E., & Bernoulli, D. (2010). Reconciling  
662 plate-tectonic reconstructions of Alpine Tethys with the geological–geophysical record of  
663 spreading and subduction in the Alps. *Earth-Science Reviews*, 102(3-4), 121-158.  
664

665 Handy, M. R., Ustaszewski, K., & Kissling, E. (2015). Reconstructing the Alps–Carpathians–  
666 Dinarides as a key to understanding switches in subduction polarity, slab gaps and surface  
667 motion. *International Journal of Earth Sciences*, 104(1), 1-26.  
668

669 Hawkesworth, C. J., Waters, D. J., & Bickle, M. J. (1975). Plate tectonics in the Eastern Alps.  
670 *Earth and Planetary Science Letters*, 24(3), 405-413.  
671

672 Hetényi, G., Plomerová, J., Bianchi, I., Exnerová, H. K., Bokelmann, G., Handy, M. R., ... &  
673 AlpArray-EASI Working Group. (2018). From mountain summits to roots: Crustal structure of  
674 the Eastern Alps and Bohemian Massif along longitude 13.3 E. *Tectonophysics*, 744, 239-255.  
675

676 Holzrichter, N., & Ebbing, J. (2016). A regional background model for the Arabian Peninsula  
677 from modeling satellite gravity gradients and their invariants. *Tectonophysics*, 692, 86-94.  
678

679 Hua, Y., Zhao, D., & Xu, Y. (2017). P wave anisotropic tomography of the Alps. *Journal of*  
680 *Geophysical Research: Solid Earth*, 122(6), 4509-4528.  
681

682 Isaak, D. G., Anderson, O. L., Goto, T., & Suzuki, I. (1989). Elasticity of single-crystal  
683 forsterite measured to 1700 K. *Journal of Geophysical Research: Solid Earth*, 94(B5), 5895-  
684 5906.  
685

686 Isaak, D. G. (1992). High-temperature elasticity of iron-bearing olivines. *Journal of*  
687 *Geophysical Research: Solid Earth*, 97(B2), 1871-1885.  
688

689 Karato, S. I. (1993). Importance of anelasticity in the interpretation of seismic tomography.  
690 *Geophysical Research Letters*, 20(15), 1623-1626.  
691

692 Karousová, H., Plomerová, J., & Babuška, V. (2013). Upper-mantle structure beneath the  
693 southern Bohemian Massif and its surroundings imaged by high-resolution  
694 tomography. *Geophysical Journal International*, 194(2), 1203-1215.  
695

696 Kästle, E. D., El-Sharkawy, A., Boschi, L., Meier, T., Rosenberg, C., Bellahsen, N., ... &  
697 Weidle, C. (2018). Surface wave tomography of the alps using ambient-noise and earthquake  
698 phase velocity measurements. *Journal of Geophysical Research: Solid Earth*, 123(2), 1770-  
699 1792.  
700

701 Kästle, E. D., Rosenberg, C., Boschi, L., Bellahsen, N., Meier, T., & El-Sharkawy, A. (2020).  
702 Slab break-offs in the Alpine subduction zone. *International Journal of Earth Sciences*, 1-17.  
703

704 Kincaid, C., & Olson, P. (1987). An experimental study of subduction and slab  
705 migration. *Journal of Geophysical Research: Solid Earth*, 92(B13), 13832-13840.  
706

707 Kissling, E., Schmid, S. M., Lippitsch, R., Ansorge, J., & Fügenschuh, B. (2006). Lithosphere  
708 structure and tectonic evolution of the Alpine arc: new evidence from high-resolution  
709 teleseismic tomography. *Geological Society, London, Memoirs*, 32(1), 129-145.  
710

711 Kogan, M. G., & McNutt, M. K. (1993). Gravity field over northern Eurasia and variations in  
712 the strength of the upper mantle. *Science*, 259(5094), 473-479.  
713

714 Koulakov, I., Kaban, M. K., Tesauro, M., & Cloetingh, S. A. P. L. (2009). P-and S-velocity  
715 anomalies in the upper mantle beneath Europe from tomographic inversion of ISC data.  
716 *Geophysical Journal International*, 179(1), 345-366.  
717

718 Le Breton, E., Handy, M. R., Molli, G., & Ustaszewski, K. (2017). Post-20 Ma motion of the  
719 Adriatic Plate: New constraints from surrounding orogens and implications for crust-mantle  
720 decoupling. *Tectonics*, 36(12), 3135-3154.  
721

722 Lippitsch, R., Kissling, E., & Ansorge, J. (2003). Upper mantle structure beneath the Alpine  
723 orogen from high-resolution teleseismic tomography. *Journal of Geophysical Research: Solid*  
724 *Earth*, 108(B8).

725

726 Lüschen, E., Lammerer, B., Gebrande, H., Millahn, K., Nicolich, R., & TRANSALP Working  
727 Group. (2004). Orogenic structure of the Eastern Alps, Europe, from TRANSALP deep seismic  
728 reflection profiling. *Tectonophysics*, 388(1-4), 85-102.

729

730 Lüschen, E., Borrini, D., Gebrande, H., Lammerer, B., Millahn, K., Neubauer, F., ... &  
731 TRANSALP Working Group. (2006). TRANSALP—deep crustal Vibroseis and explosive  
732 seismic profiling in the Eastern Alps. *Tectonophysics*, 414(1-4), 9-38.

733

734 Lyu, C., Pedersen, H. A., Paul, A., Zhao, L., & Solarino, S. (2017). Shear wave velocities in  
735 the upper mantle of the Western Alps: new constraints using array analysis of seismic surface  
736 waves. *Geophysical Journal International*, 210(1), 321-331.

737

738 Mahatsente, R. (2019). Plate Coupling Mechanism of the Central Andes Subduction: Insight  
739 from Gravity Model. *Journal of Geodetic Science*, 9(1), 13-21.

740

741 McDonough, W. F., & Sun, S. S. (1995). The composition of the Earth. *Chemical geology*,  
742 120(3-4), 223-253.

743

744 McKenzie, D., & Fairhead, D. (1997). Estimates of the effective elastic thickness of the  
745 continental lithosphere from Bouguer and free air gravity anomalies. *Journal of Geophysical*  
746 *Research: Solid Earth*, 102(B12), 27523-27552.

747

748 Mitterbauer, U., Behm, M., Brückl, E., Lippitsch, R., Guterch, A., Keller, G. R., ... &  
749 Šumanovac, F. (2011). Shape and origin of the East-Alpine slab constrained by the ALPASS  
750 teleseismic model. *Tectonophysics*, 510(1-2), 195-206.

751

752 Nocquet, J. M., & Calais, E. (2004). Geodetic measurements of crustal deformation in the  
753 Western Mediterranean and Europe. *Pure and applied geophysics*, 161(3), 661-681.

754

755 Piromallo, C., & Morelli, A. (2003). P wave tomography of the mantle under the Alpine -  
756 Mediterranean area. *Journal of Geophysical Research: Solid Earth*, 108(B2).

757

758 Reuber, G., Meier, T., Ebbing, J., El-Sharkawy, A., & Kaus, B. (2019, January). Constraining  
759 the dynamics of the present-day Alps with 3D geodynamic inverse models-model version 0.2.  
760 In *Geophysical Research Abstracts (Vol. 21)*.

761

762 Root, B. C. (2020). Comparing global tomography-derived and gravity-based upper mantle  
763 density models. *Geophysical Journal International*, 221(3), 1542-1554.

764

765 Schmid, S. M., Fügenschuh, B., Kissling, E., & Schuster, R. (2004). Tectonic map and overall  
766 architecture of the Alpine orogen. *Eclogae Geologicae Helveticae*, 97(1), 93-117.

767

768 Serpelloni, E., Vannucci, G., Anderlini, L., & Bennett, R. A. (2016). Kinematics,  
769 seismotectonics and seismic potential of the eastern sector of the European Alps from GPS and  
770 seismic deformation data. *Tectonophysics*, 688, 157-181.

771

772 Spada, M., Bianchi, I., Kissling, E., Agostinetti, N. P., & Wiemer, S. (2013). Combining  
773 controlled-source seismology and receiver function information to derive 3-D Moho  
774 topography for Italy. *Geophysical Journal International*, 194(2), 1050-1068.  
775

776 Spakman, W., & Wortel, R. (2004). A tomographic view on western Mediterranean  
777 geodynamics. In *The TRANSMED atlas. The Mediterranean region from crust to mantle* (pp.  
778 31-52). Springer, Berlin, Heidelberg.  
779

780 Spooner, C., Scheck-Wenderoth, M., Götze, H. J., Ebbing, J., & Hetényi, G. (2019). Density  
781 distribution across the Alpine lithosphere constrained by 3-D gravity modelling and relation to  
782 seismicity and deformation. *Solid Earth*, 10(6), 2073-2088.  
783

784 Stampfli, G. M., & Borel, G. D. (2002). A plate tectonic model for the Paleozoic and Mesozoic  
785 constrained by dynamic plate boundaries and restored synthetic oceanic isochrons. *Earth and  
786 Planetary Science Letters*, 196(1-2), 17-33.  
787

788 Tadiello, D., & Braitenberg, C. (2021). Gravity modeling of the Alpine lithosphere affected by  
789 magmatism based on seismic tomography. *Solid Earth Discussions*, 1-31.  
790

791 Tašárová, Z. A. (2007). Towards understanding the lithospheric structure of the southern  
792 Chilean subduction zone (36 S–42 S) and its role in the gravity field. *Geophysical Journal  
793 International*, 170(3), 995-1014.  
794

795 Tiberi, C., Diament, M., Lyon Caen, H., & King, T. (2001). Moho topography beneath the  
796 Corinth Rift area (Greece) from inversion of gravity data. *Geophysical Journal  
797 International*, 145(3), 797- 808.  
798

799 Uieda, L., Barbosa, V. C., & Braitenberg, C. (2016). tesserooids: Forward-modeling  
800 gravitational fields in spherical coordinates. *Geophysics*, 81(5), F41-F48.  
801

802 Vacher, P., Mocquet, A., & Sotin, C. (1998). Computation of seismic profiles from mineral  
803 physics: the importance of the non-olivine components for explaining the 660 km depth  
804 discontinuity. *Physics of the Earth and Planetary Interiors*, 106(3-4), 275-298.  
805

806 Vrabc, M., & Fodor, L. (2006). Late Cenozoic tectonics of Slovenia: structural styles at the  
807 Northeastern corner of the Adriatic microplate. In *The Adria microplate: GPS geodesy,  
808 tectonics and hazards* (pp. 151-168). Springer, Dordrecht.  
809

810 Wang, Y., He, Y., Lu, G., & Wen, L. (2020). Seismic, thermal and compositional structures of  
811 the stagnant slab in the mantle transition zone beneath southeastern China. *Tectonophysics*,  
812 775, 228208.  
813

814 Webb, S. J. (2009). The use of potential field and seismological data to analyze the structure of  
815 the lithosphere beneath southern Africa (Doctoral dissertation).  
816

817 Wessel, P., Smith, W. H., Scharroo, R., Luis, J., & Wobbe, F. (2013). Generic mapping tools:  
818 improved version released. *Eos, Transactions American Geophysical Union*, 94(45), 409-410.  
819

820 Wessel, P., & Luis, J. F. (2017). The GMT/MATLAB Toolbox. *Geochemistry, Geophysics,  
821 Geosystems*, 18(2), 811-823.  
822

823 Workman, R. K., & Hart, S. R. (2005). Major and trace element composition of the depleted  
824 MORB mantle (DMM). *Earth and Planetary Science Letters*, 231(1-2), 53-72.

825  
826 Zeyen, H., & Fernández, M. (1994). Integrated lithospheric modeling combining thermal,  
827 gravity, and local isostasy analysis: Application to the NE Spanish Geotranssect. *Journal of*  
828 *Geophysical Research: Solid Earth*, 99(B9), 18089-18102.

829  
830 Zhao, L., Paul, A., Malusà, M. G., Xu, X., Zheng, T., Solarino, S., ... & Aubert, C. (2016).  
831 Continuity of the Alpine slab unraveled by high-resolution P wave tomography. *Journal of*  
832 *Geophysical Research: Solid Earth*, 121(12), 8720-8737.

833  
834 Zingerle, P., Pail, R., Gruber, T., & Oikonomidou, X. (2020). The combined global gravity field  
835 model XGM2019e. *Journal of Geodesy*, 94(7), 1-12.

836

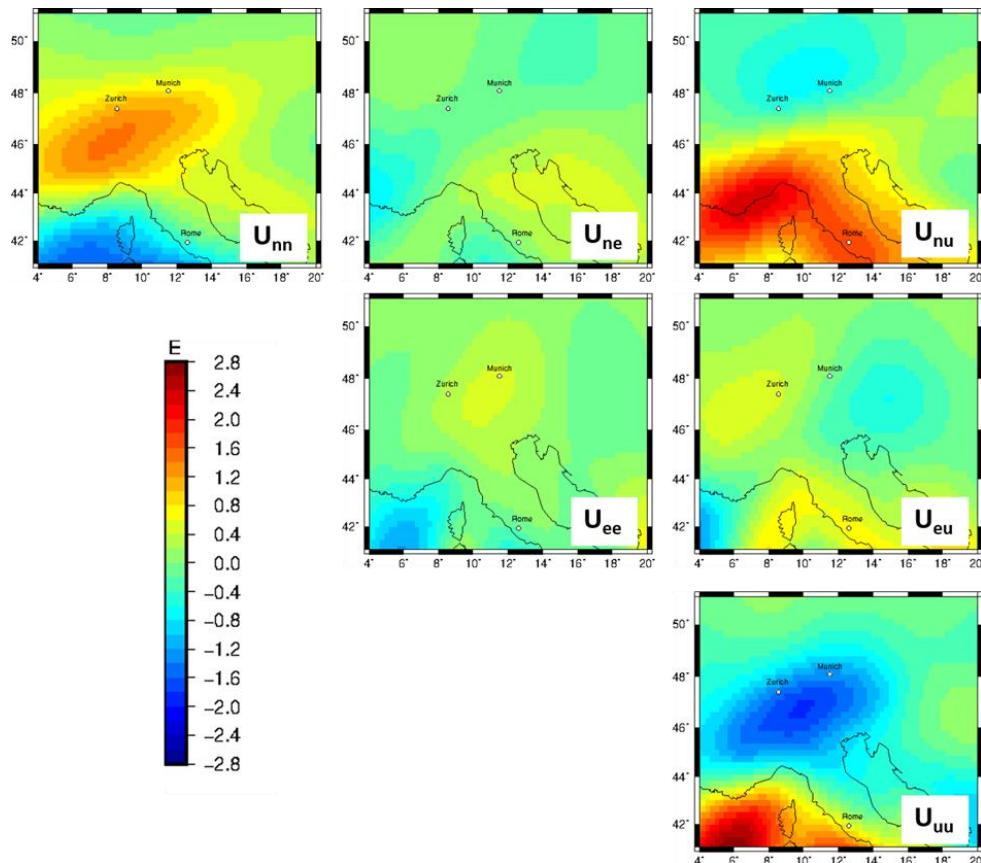
### 837 **Appendix A Gravity Gradients at satellite height**

838 For all Alpine density models presented above (section 3, 4.1 and 4.2) we have also calculated  
839 gravity gradients at a station height of 225 km. This station height corresponds to the second  
840 mission phase of GOCE (Gravity field and steady-state ocean circulation explorer) carried out  
841 by ESA (European Space Agency).

842 We anticipated that gravity gradients measured by the GOCE satellite mission are sensitive to  
843 the slab segments in the Alpine region. Our result show, that the long wavelength signal of the  
844 different present slab segments contributes to a large-scale gravity response where the different  
845 contributor cannot be separated. Therefore, we conclude that against our anticipation gravity  
846 gradients at satellite height are in fact not sensitive to the Alpine slab configuration. We show  
847 here, the gravity gradients (mainly the gzz component) for completeness.

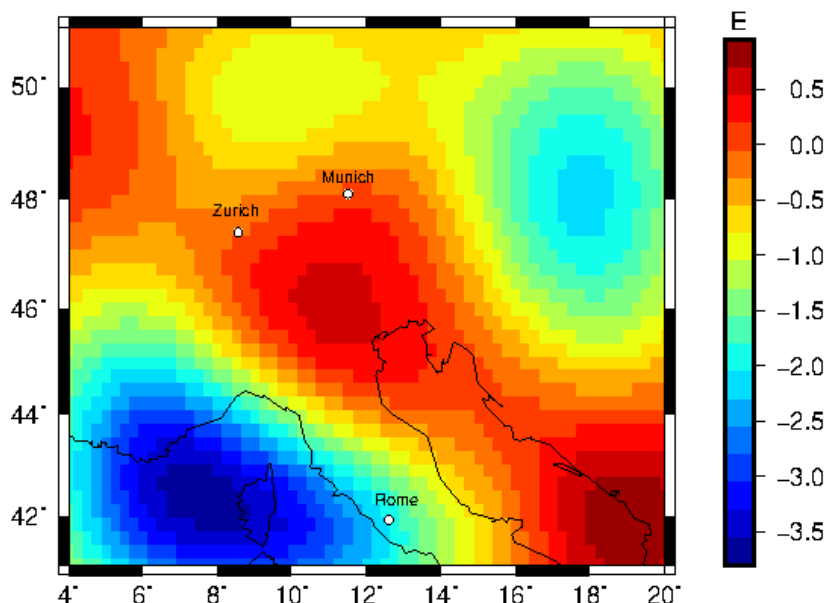
848 Measured gravity gradients from the GOCE mission (Bouman et al., 2016), which were  
849 corrected for topography and bathymetry ranges from 2.5 to -2.5 E at satellite altitude of 225  
850 km height (Fig. 13). A negative gravity anomaly of -2.5 E in the gzz component is observed  
851 equivalent to the vertical gz component (Fig. 13). However, no clear sign for subducting  
852 lithosphere can be observed in any component of the gravity gradient tensor.





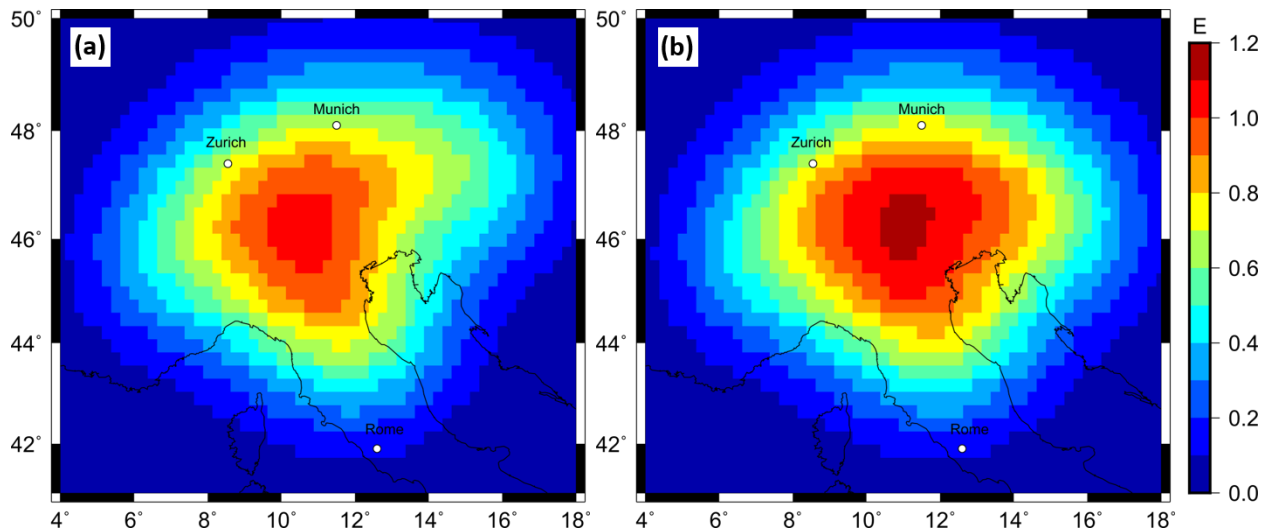
853  
 854 *Figure 13 GOCE gradients at 225 km height after Bouman et al. (2016) corrected for topography and bathymetry with a 5°*  
 855 *extension to remove far field effects. The gravity gradients are presented in a North-East-Up coordinate system.*

856 The forward calculated gzz component at 225 km station height from a density model (section  
 857 3) with converted densities ranges from -3.5 E to 0.7 E (Fig. 14). A positive gravity signal of  
 858 about 0.5 E in the Apennine and Alpine region is observed which could be linked to subducting  
 859 slab segments. However, it is impossible to separate specific slab segments.



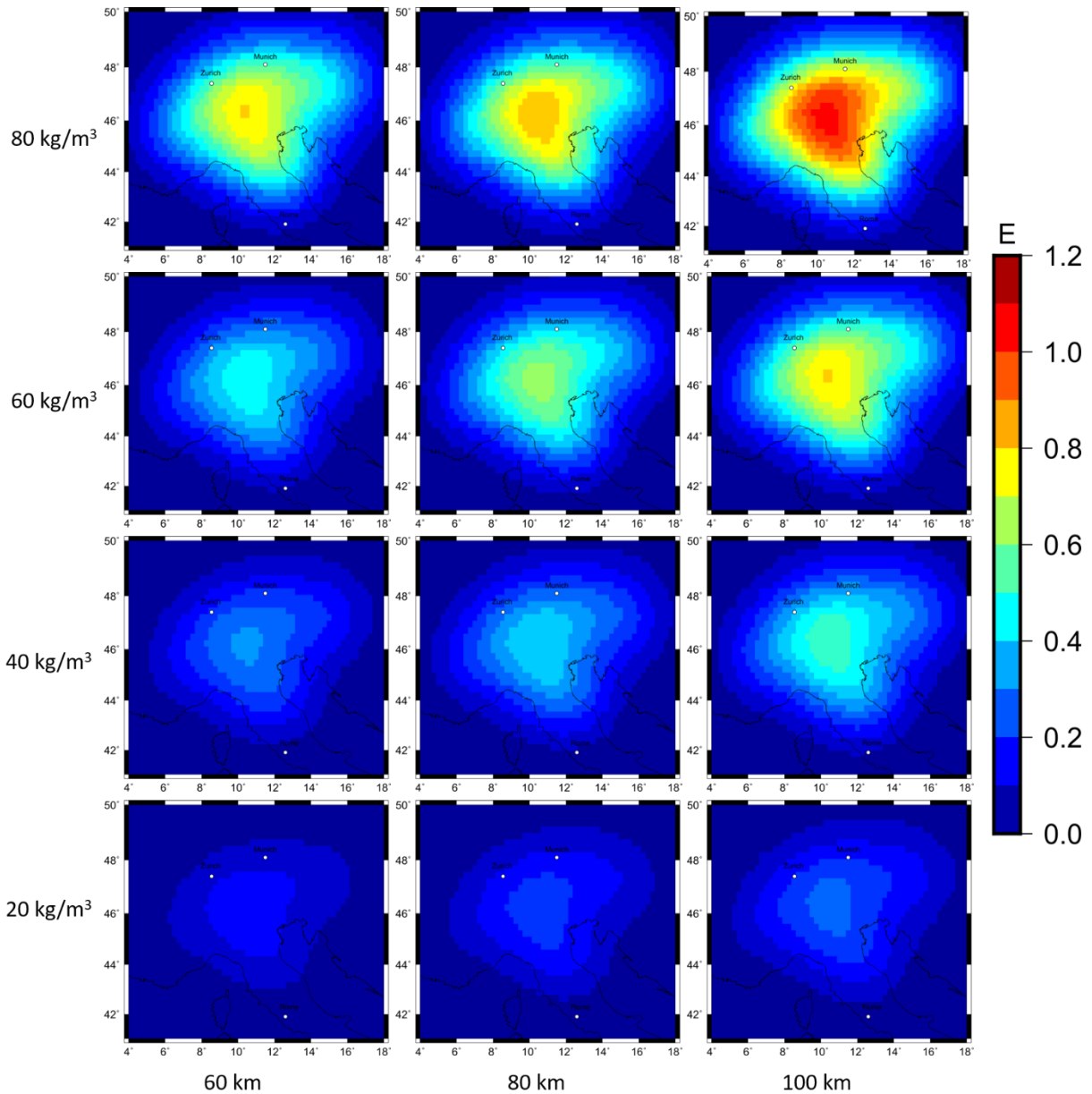
860  
 861 *Figure 14 Forward calculated gzz gravity signal from relative density distribution converted from relative seismic velocities*  
 862 *using a conversion factor of 0.3 for the at 225 km station height.*

863 Forward calculated tesseroïd models (section 4.1) for slab configuration 1 and 2 with a constant  
 864 density contrast of  $60 \text{ kg/m}^3$  and a constant thickness of 80 km result in a less sharp gravity  
 865 signal for the gzz component at a station height of 225 km (Fig. 15) compared to the gz  
 866 component at station height of 6040 m (Fig. 6). The gravity signal for the gzz component is in  
 867 the range of 0.8 E to 1 E. At satellite altitude the gravity signal is observed as a large area with  
 868 a positive gravity effect for Configuration 1 and 2. The contribution of the different slab  
 869 segments to this positive gravity effect is not distinguishable. The only recognizable difference  
 870 is the size of this positive gravity signal. Configuration 1 shows a smaller anomaly, due to a  
 871 lower volume of subducting material in the Eastern Alps.



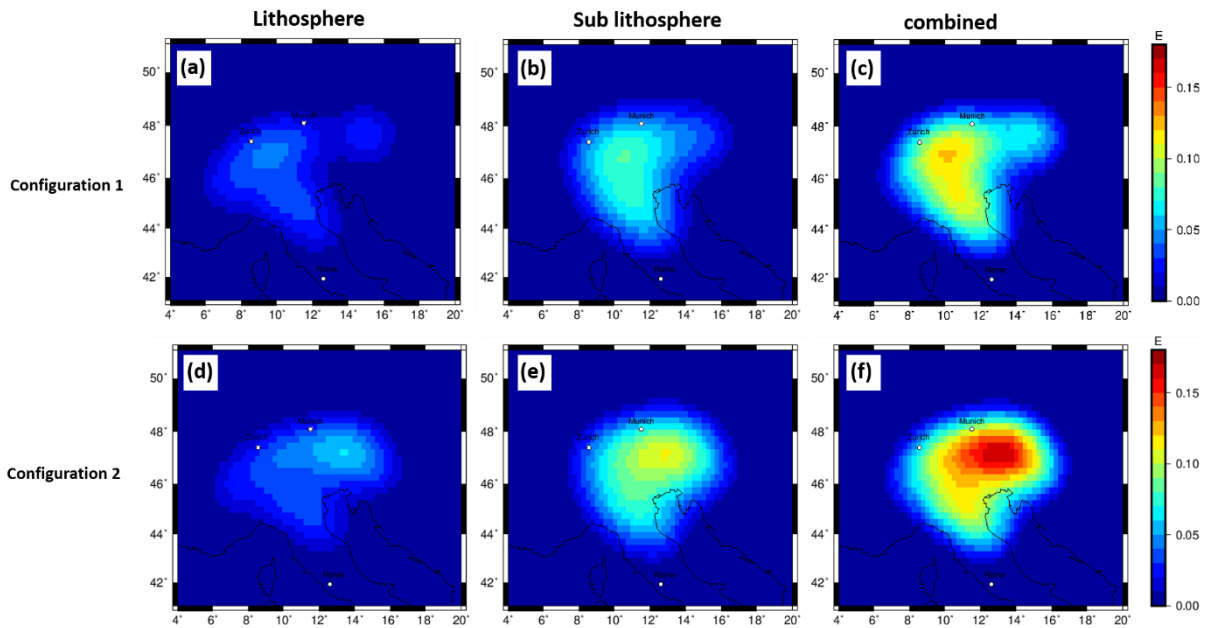
872  
 873 *Figure 15 Forward calculated gzz gravity signal at a station height of 225 km from predefined sub-crustal slab geometries with*  
 874 *a content density contrast of  $60 \text{ kg/m}^3$  and a constant thickness of 80 km. (a) slab configuration of hypothesis 1 (b) slab*  
 875 *configuration of hypothesis 2.*

876 In Addition, the signal strength for the forward calculated gzz component show the same  
 877 dependency of signal strength to the density contrast and slab thickness (Fig. 16) as the gz  
 878 component (Fig. 7). The signal strength of the gzz component ranges for the 12 different  
 879 combinations from 0.3 E to 2 E (Fig. 16). The gravity signal cannot be separated and affiliated  
 880 to a certain slab segment. The gzz gradient signal shows a large blurry gravity high over the  
 881 Alps, which thins out to the edges.

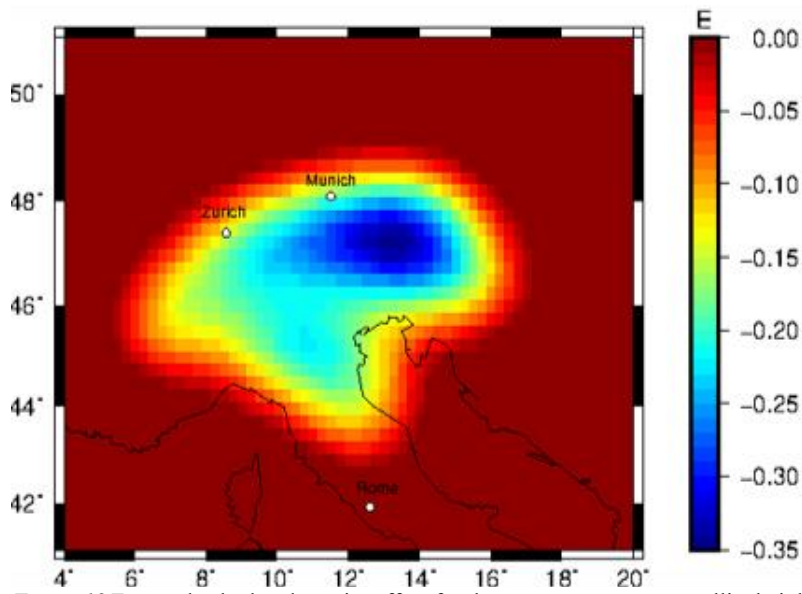


882  
 883 *Figure 16 Forward calculated gzz gravity signal for 12 different combination of density contrast and slab thickness at a station*  
 884 *height of 225 km for sub-crustal slab configuration 1.*

885 The gravity effect for the LitMod models (section 4.2) with the slab Configuration 1 shows in  
 886 the lithosphere domain a signal strength of about 0.05 E, while the sub lithospheric gravity  
 887 signal is in the range of 0.1 E for the gzz component at satellite altitude of 225 km height. The  
 888 combined gravity signal is in the order of 0.14 E (Fig. 17). A Proterozoic slab produces a larger  
 889 amplitude in signal strength, however the different slab segments can again not be separated  
 890 (Fig. 18).



891  
 892  
 893  
 894  
 895  
 Figure 17 forward calculated gzz gravity signal at satellite altitude of 225 km based on LitMod models with tecton like compositions in the lithosphere and PUM and DMM compositions in the sub lithosphere ( $M_1, M_2, M_3, M_4$ ) with an additional thermal anomaly of  $-100^\circ K$  for the sub-lithospheric slab segment, for predefined slab Configuration to the background model  $M_0$ . (a)-(c) for Configuration 1. (d)-(f) for Configuration 2. Topographic and crustal effects are nullified.



896  
 897  
 898  
 899  
 Figure 18 Forward calculated gravity effect for the gzz component at satellite height of a Proterozoic lithospheric slab segment to a Tecton compositional surrounding mantle for Configuration 2 obtained by calculating the residual between  $M_8$  and  $M_0$ .